

# Variation in Pore Structure and Associated Fractal Dimensions of Barakar and Barren Measures Carbon-Rich Gas Shales of Jharia Basin, India

Ranjit Gangadhar Khangar, Vinod Atmaram Mendhe,\* Alka Damodhar Kamble, Piyush Ranjan Das, Priyanka Shukla, Mollika Bannerjee, and Atul Kumar Varma

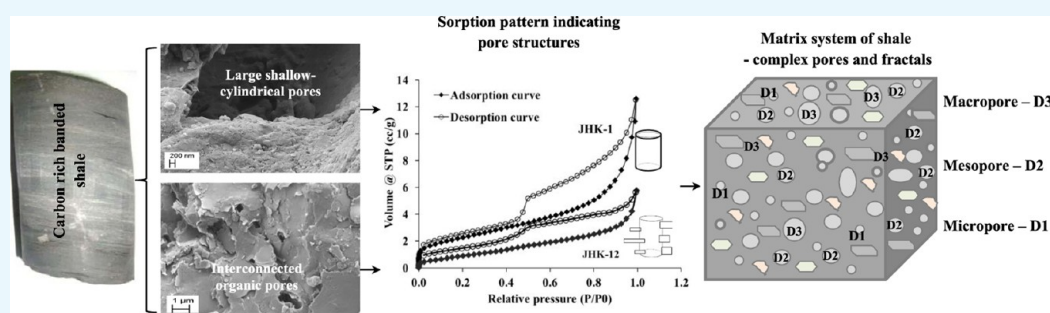
Cite This: *ACS Omega* 2021, 6, 28678–28698

Read Online

ACCESS |

Metrics & More

Article Recommendations



**ABSTRACT:** The carbon-rich Barakar and Barren Measures shale beds of the Jharia basin were evaluated for variation in pore size, pore structure, and fractal dimensions. The shale core samples were obtained from exploratory boreholes drilled at the Jharia basin. The shale samples were analyzed for organo-inorganic composition by FTIR, pore size, and pore structure using BET low-pressure  $N_2$  adsorption and pore geometry through FE-SEM photographs. The shale samples have significant carbon-rich content and are intercalated-banded in nature. The pore structures were evaluated through  $N_2$  isotherms and validated by SEM images, revealing the mixed contribution of organo-inorganic matter in pore formations controlled by geochemical alteration, diagenesis, and mineral interaction. The rough internal surfaces of the pore were evaluated by categorizing them into fractals  $D_1$ ,  $D_2$ , and  $D_3$ . It is observed that the  $D_2$  type of fractals is in abundance associated with mesopores. The positive trend of fractals with pore size, pore structure, depth, fixed carbon, and TOC suggests the influence of different parameters on the formation of pore internal rugged surfaces in shale beds. The FE-SEM images indicate shallow to deep pores with different pore structures with fair to good pore connectivity. In summary, the shale beds of Jharia have heterogeneous complex pore structures, a rough surface, and sorption mechanisms controlled by weathering/alteration, depositional conditions, and organo-inorganic content. In shale beds, gas storage and transport phenomena are directly related to pore size distribution, pore structure, and associated fractal dimensions. The calculated values using the proposed empirical models for porosity ( $EPO_f$ ) and permeability ( $EPE_f$ ) showed excellent linear correlation with the measured porosity (MPOc,  $R^2 = 0.8577$ ) and permeability (MPEC,  $R^2 = 0.8577$ ), which are close to measured values. The curve matching of  $EPO_f$  with MPOc and  $EPE_f$  with MPEC follows a similar path, validating the results and suitability of the models. Hence, the proposed models may be considered to estimate the porosity and permeability of shale and coal beds.

## 1. INTRODUCTION

Shale gas is a natural gas, which dominantly contains methane derived from shale deposits.<sup>1–5</sup> The world energy scenario has rapidly changed in the past few decades due to the shale gas revolution. New technologies of horizontal drilling and hydraulic fracturing have paved the way for the United States to become an oil and gas exporter.<sup>8–10</sup> It has also changed the energy and fossil-fuel-governing geopolitics of the world.<sup>1,6–10</sup> The shale matrix has complex systems of pores of different sizes from micro-, meso-, and macropores attributed to a heterogeneous mix of organo-inorganic content.<sup>4,11–16,89,90</sup> The gas storage and release mechanism in shale depends on pore type,

pore structure, pore size, and pore fractals.<sup>2,17–19,88</sup> The shale matrix pore types and pore structures are mainly influenced by depositional conditions, clay type, moisture, and volatile matter content.<sup>5,88</sup> Likewise, pore surface formation can be contingent on the cracking of organic compounds, pore evolution, stages of

Received: June 25, 2021

Accepted: September 30, 2021

Published: October 21, 2021



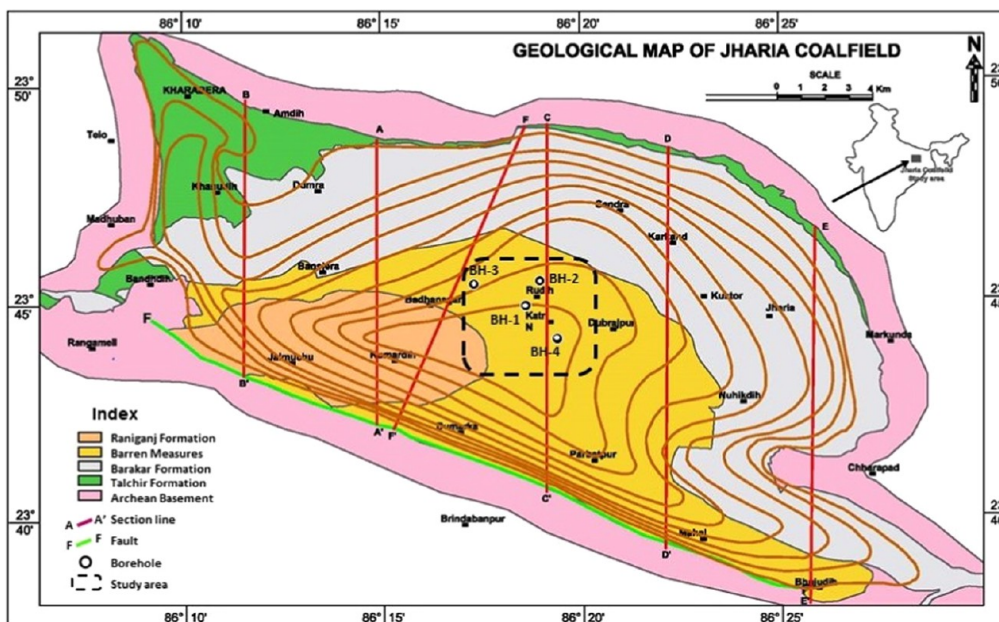


**Figure 1.** Geological map of the Jharia coalfield showing the study area and shale core sampling borehole locations<sup>53</sup> (reprinted in part with permission from Elsevier-Publisher; Verma et al., 1979). [Verma, R. K.; Bhui, N. C.; Mukhopadhyay, M. *Geology, Structure and tectonics of Jharia CoalField, India-A 3-D Model. Geoexploration* 1979, 17, 305–324].

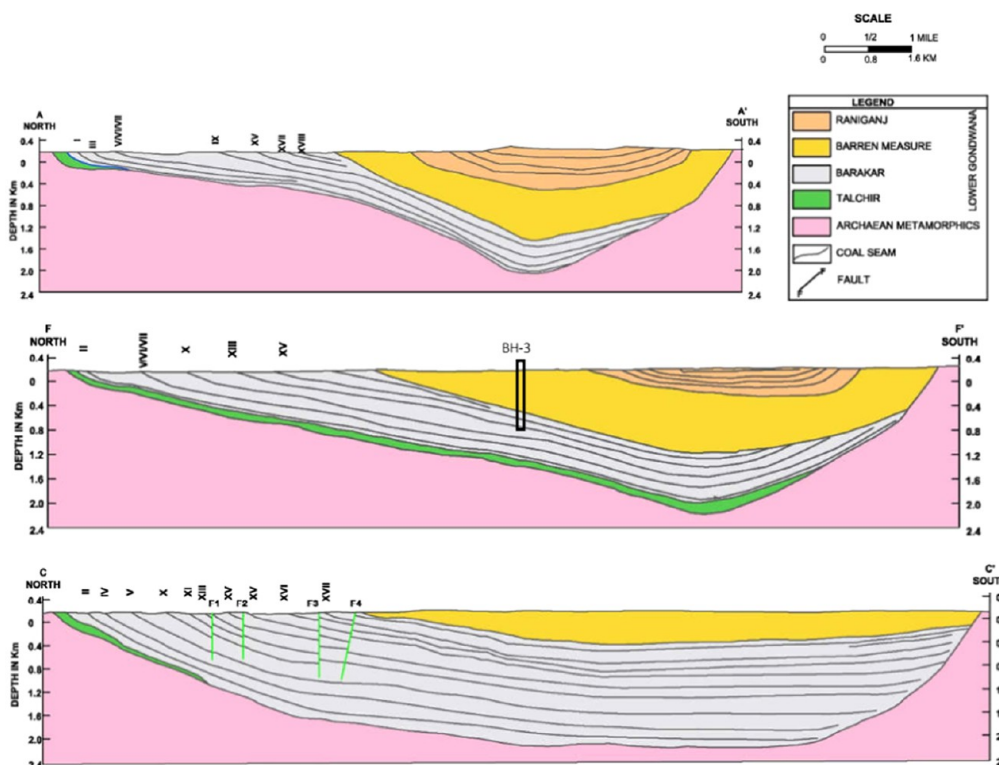







**Figure 2.** Profile and cross sections based on gravity and borehole data along the section lines in the geological map of the Jharia basin<sup>53</sup> (reprinted in part with permission from Elsevier-Publisher; Verma et al., 1979). [Verma, R. K.; Bhui, N. C.; Mukhopadhyay, M. *Geology, Structure and tectonics of Jharia CoalField, India-A 3-D Model. Geoexploration* 1979, 17, 305–324].

compactions, and thermal maturity.<sup>20–23</sup> Fourier transform infrared spectroscopy (FTIR) provides crucial information about the functional groups present in shale. The absorption peaks also show the clay and mineral matters<sup>24–31</sup> and the kerogen transformation level.<sup>32–37</sup> It also provides information on the transformation of the aliphatic to aromatic components due to the organic content and thermal maturation.<sup>4,22,26,30</sup>

In India, shale gas exploration and its commercial recovery are emerging as a clean energy resource development. The government is looking for improvements in shale gas development to reduce its petroleum import and dependence and fulfill the growing energy needs of 1.25 billion people.<sup>38,39</sup> The Proterozoic, Gondwana, and Tertiary sedimentary basins in India have been assessed for shale gas potential and estimated 63 tcf of

Table 1. Stratigraphic Succession of the Jharia Basin<sup>55</sup> (Modified after Mukhopadhyay et al., 2010)

Age (Ma)	System/Period	Series/Epoch	Stage/Age	Formation/Thickness	Lithology
66 110	Cretaceous			Igneous Intrusive	Basaltic dykes and sills
Unconformity					
252	Upper Permian	Lopingian	Canghsingian	Raniganj (800 m)	Fine to medium grained greenish sandstone with shale and coal seams
			Wachiapingian		
260	Middle Permian	Guadalupian	Wordian	Barren Measures (730m)	Clay-rich and carbon-rich shale dominated hetero-lithic sequence. Massive sandstone
					
271 290	Lower Permian	Cisularian	Kungurian	Barakar (1250 m)	Dirty white coarse and medium grained feldspathic sandstones, grits, grey shale, carbon-rich shale with coal seams
			Artinskian		
			Asselian		
299 302	Upper Carboniferous		Gzhellian	Talchir (245 m)	White coarse grained sandstone, green shales and fine grained sandstone, conglomerate lenses and basal tillite
					
Unconformity					
	Pre-cambrian			Chotanagpur Complex	Granite gneiss, hornblende schist/gneiss, metabasic rocks, pegmatite and quartz veins etc.
					

recoverable resources.<sup>8</sup> The exploration and exploitation of Gondwana coal in India have continued since 1774.<sup>3,40</sup> However, associated shales were considered seal (cap-rock) and not a resource; hence, scientific documentation has never been done.<sup>38–40</sup> Presently, gathering information on fundamental shale gas reservoir characteristics is in full swing in India. The coal seams of the Jharia basin are placed in Category-I, known for maximum future commercial methane potential among Indian CBM blocks. There are thick shale horizons in Barren Measures and the strata between coal seams of the Barakar Formation. The micro properties of these shales are yet to be understood. In this study, the carbon-rich Barakar and Barren Measures shale beds of the Jharia basin have been evaluated for variation in pore size, pore structure, and fractal dimensions with significance to gas storage.

This study attempted an analysis of the pore structure, associated fractal dimensions, and sorption mechanism variation in thick shale sequences of Barakar and Barren Measures Formation of the Jharia basin. Clay-associated pores significantly store methane and play an important role in the adsorption and desorption phenomena in shale.<sup>41–44</sup> The gas flow in shale rocks is governed mainly by clay containing a pore network by the non-Darcy effects.<sup>4,45,46</sup> Therefore, the porosity and permeability of shale depend on clay type and mineral content. Low-pressure N<sub>2</sub> adsorption/desorption isotherms and their hysteresis patterns provide helpful information about the physisorption mechanism, surface area, pore volume, pore

size, and pore structure characteristics of the shale/coal.<sup>45,46</sup> The fractal dimensions derived following FHH models indicated a complex fractal system associated with a matrix containing micro-, meso-, and macropores. The hysteresis patterns corresponding to the shale sample correlate with the pore structure identified with scanning electron microscopy (SEM). The study provides insights into the variation of organo-inorganic formed pores, pore structures, surface area, and fractal dimensions regarding shale gas storage and the recovery mechanism.

## 2. GEOLOGY OF THE JHARIA BASIN

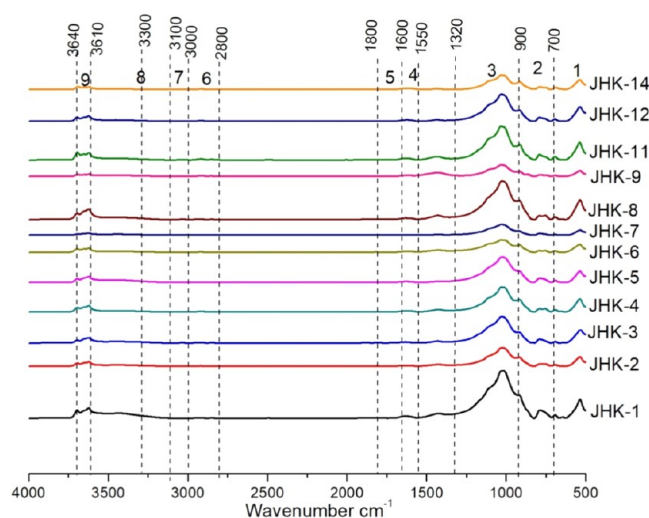
Jharia is one of the most prospective coking coal-bearing basins of the Damodar valley, Jharkhand, and stretches over 450 km<sup>2</sup>.<sup>47</sup> It lies between latitudes 23°37' and 23°52' and longitudes 86°06' and 86°30'. It occurs in a "half-graben" structure,<sup>48,49</sup> trending in an east–west direction and plunging in the west curtailed by a key fault at the southern boundary having over 1500 m throw.<sup>50–52</sup> The geological map of the Jharia basin showing the study area and shale core sampling boreholes is given in Figure 1.<sup>53</sup> The profile and cross sections based on gravity and borehole data along the section lines in the geological map of the Jharia basin have been modified after<sup>53</sup> and are given in Figure 2. The Jharia basin is roughly sickle-shaped, and the dip of the formations usually is 10 ± 5°. The lineament corresponding to the depositional belt has been considered a predepositional zone of weakness with syntectonic activity<sup>48</sup> others have considered it postdepositional faults.<sup>54</sup>



Table 2. Results of FTIR Analysis of Shale Core Samples<sup>a</sup>

sample no.	formation	OHstretching/ phyllosilicate	hydroxyl group	C–C stretch/kerogen	aromatic C=C	carbonates	kaolinite	Si–O stretching/quartz	A-factor	C-factor	IAL	IAR
JHK-1	Barren	✓	–	–	✓	✓	✓	✓	0.42	0.54	0.35	0.53
JHK-2	Measures	✓	–	✓	✓	✓	✓	✓	0.38	0.41	0.24	0.62
JHK-3		✓	–	✓	✓	✓	✓	✓	0.41	0.17	0.20	0.45
JHK-4		✓	–	✓	✓	✓	✓	✓	0.35	0.07	0.03	0.61
JHK-5		✓	–	✓	✓	✓	✓	✓	0.52	0.38	0.21	0.55
JHK-6		✓	–	✓	✓	✓	✓	✓	0.38	0.24	0.13	0.48
JHK-7	Barakar	✓	–	✓	✓	✓	✓	✓	0.34	0.32	0.18	0.62
JHK-8		✓	–	✓	✓	✓	✓	✓	0.18	0.26	0.14	0.51
JHK-9		✓	–	✓	✓	✓	✓	✓	0.32	0.29	0.16	0.48
JHK-10		✓	–	✓	✓	✓	✓	✓	0.29	0.29	0.16	0.45
JHK-11		✓	–	✓	✓	✓	✓	✓	0.30	0.27	0.15	0.38
JHK-12		✓	–	✓	✓	✓	✓	✓	0.44	0.38	0.15	0.64
JHK-13		✓	–	✓	✓	✓	✓	✓	0.36	0.19	0.10	0.47
JHK-14		✓	–	✓	✓	✓	✓	✓	0.42	0.18	0.08	0.52
JHK-15		✓	–	✓	✓	✓	✓	✓	0.49	0.41	0.22	0.56

<sup>a</sup>Explanations: A-factor =  $\{(2940 + 2850) \text{ cm}^{-1}/(2940 + 2850 + 1604) \text{ cm}^{-1}\}$ ; C-factor =  $\{1740 \text{ cm}^{-1}/(1740 + 1604) \text{ cm}^{-1}\}$ ; IAL, aliphaticity index; IAR, aromaticity index.



**Figure 3.** FTIR spectra showing different stretchings of aliphatic and aromatic chains in shale samples of the Jharia basin. (1) C–Br stretch, alkyl halides. (2) Aromatic CH<sub>x</sub> out-of-plane deformation. (3) C–O stretch. (4) Aromatic carbon C=C. (5) Oxygenated groups. (6) Aliphatic CH<sub>x</sub> stretching. (7) Aromatic CH<sub>x</sub> stretching. (8) O–H stretch, hydrogen-bonded. (9) O–H stretch, free hydroxyl.

According to Varma et al.,<sup>55</sup> internal basin tectonics played a significant role in folding the formations. The gradual decrease

in thickness of the Barakar formation can be observed from the east to the west. The maximum thickness of the Barren Measures has been recorded in the central part of the basin, decreasing westward and eastward. The stratigraphic succession of the Jharia basin, modified after<sup>55,56</sup> showing the lower Gondwana sequence comprising shale and coal horizons, is presented in Table 1.

### 3. RESULTS AND DISCUSSION

**3.1. Organo-Inorganic Composition by FTIR Spectroscopy.** The results of FTIR analysis of shale core samples are offered in the tabular form showing the presence of O–H stretching, C–C stretch, C=C, carbonates, kaolinite, Si–O stretching, etc. (Table 2). Organic matter in shale is a complex mix of components of numerous physico-chemical assets shown by FTIR spectra, which replicate features inbred from the original organic matter and also assimilated during subsequent diagenesis.<sup>5,11,34,57,58</sup> The facets of the microscopic organic constituents (macerals) of shale/coal are fundamental in defining economic utility, oil and gas-generating potential, and a congregation of other properties. The small peaks between 3610 and 3640 cm<sup>-1</sup> indicate the hydrous kaolinite intermixed with organic compound hydroxyl (O–H) groups. The O–H stretch of hydrogen bond (3300 cm<sup>-1</sup>) with aliphatic to aromatic chain signifies the organic matter thermal gas genesis pattern in shale. The minor peak of aromatic stretch (CH<sub>x</sub>) at 3100–3000 cm<sup>-1</sup> indicates initiation of aromatization at an early

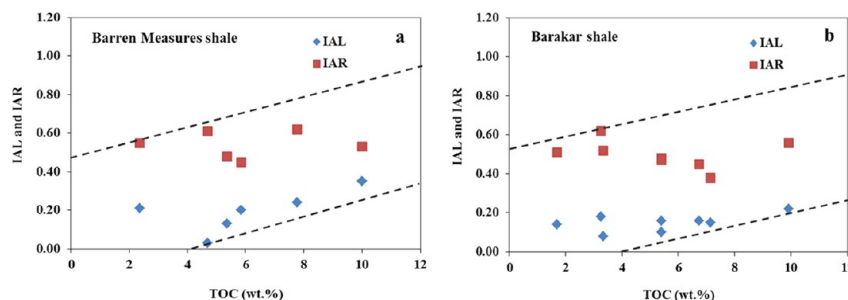


**Figure 4.** Relation of IAL and IAR with TOC content in shale, (a) Barren Measures and (b) Barakar Formations. IAL, aliphaticity index; IAR, aromaticity index; TOC, total organic carbon.

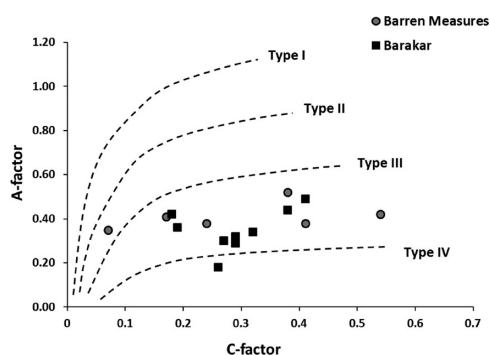


**Figure 5.** Relation of A-factor and C-factor derived from FTIR analysis of shale showing the presence of mainly type III/IV kerogen<sup>32</sup> (after Ganz and Kalkreuth, 1987). [Ganz, H.; Kalkreuth, W. Application of infrared spectroscopy to the classification of kerogen types and the evolution of source rock and oil shale potentials. *Fuel* 1987, 66, 708–711].

stage under reducing conditions. The annihilation of the aliphatic chain can be attributed to the aromatic constituents' enrichment at the peak of  $2800\text{ cm}^{-1}$ . The CO stretch of carbonates associated with oxygenated groups is shown at the peak of  $1800\text{ cm}^{-1}$ . It accentuates the aggregation of secondary mineral carbonates due to the increase in salinity approaching dry conditions in macropores and fractures of shale. The well-developed aromatic chain with trivial absorption ( $\text{C}=\text{C}$ ) recorded between  $1600$  and  $1550\text{ cm}^{-1}$  specifies that the studied shale passed through the moderate stage of thermal maturation (Figure 3).

The distinct peak of C–O of organic compounds, mainly the aromatic chain, indicates the significant conversion of aliphatic components to aromatic (oil/gas) accentuated by the liberation of volatiles and dry gases through organo-inorganic pores. Also, the more or less uniform symmetric peaks observed between  $1250$  and  $1000\text{ cm}^{-1}$  denote the deformation of the  $-\text{CH}_3$  group during alteration of aliphatic to aromatic components.<sup>59–62</sup> The peaks of aromatic regions between  $900$  and  $750\text{ cm}^{-1}$  illustrate the removal of aromatic substitutes while attaining the thermal maturity  $>1.20\%$  (bituminous stage) resulting upsurge in the aromatic condensation. Further, it is concluded that the substantial aromatization show a very good gas genesis pattern in shale, and it might have been stored in the pore-associated matrix system.<sup>58,63,64</sup> During the late stage of aromatization, the hydrous kaolinite clay and the moisture interacted with the organic matter. Hence, the water influx from the associated aquifer further alters the organic matter as a geochemical alteration. The visible peaks of kaolinite at stretch  $500\text{ cm}^{-1}$  and quartz (silicates) at  $650\text{--}700\text{ cm}^{-1}$  confirm that the active geochemical process played a vital role in altering the sediments during postdepositional conditions from diagenesis to cata- and meta-genesis phases (Figure 3).<sup>25,65–68</sup>

The FTIR spectra have been used to draw the indications on thermal maturity and kerogen type in the studied shale. The comparative ratio of aliphatic and aromatic bands is defined as the A-factor. A part of a carbonyl or carboxyl and the aromatic bands are calculated as the C-factor following the equation suggested by ref 69.

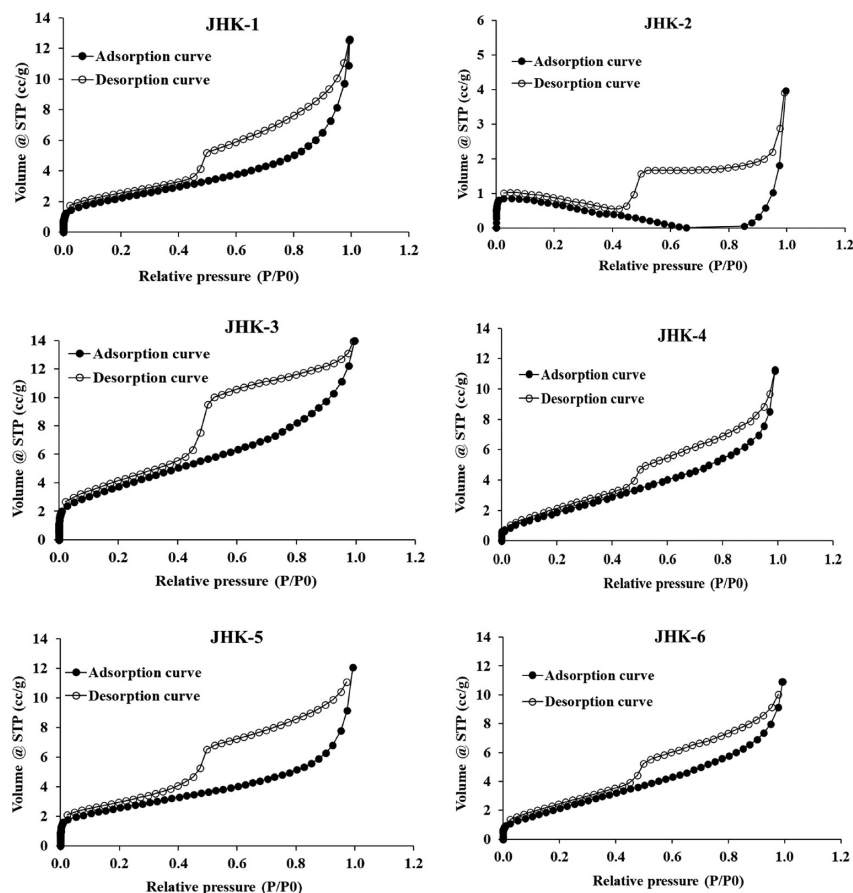


**Figure 6.** Adsorption and desorption curve showing variation in the hysteresis pattern due to different pore structures in Barren Measures shale samples.

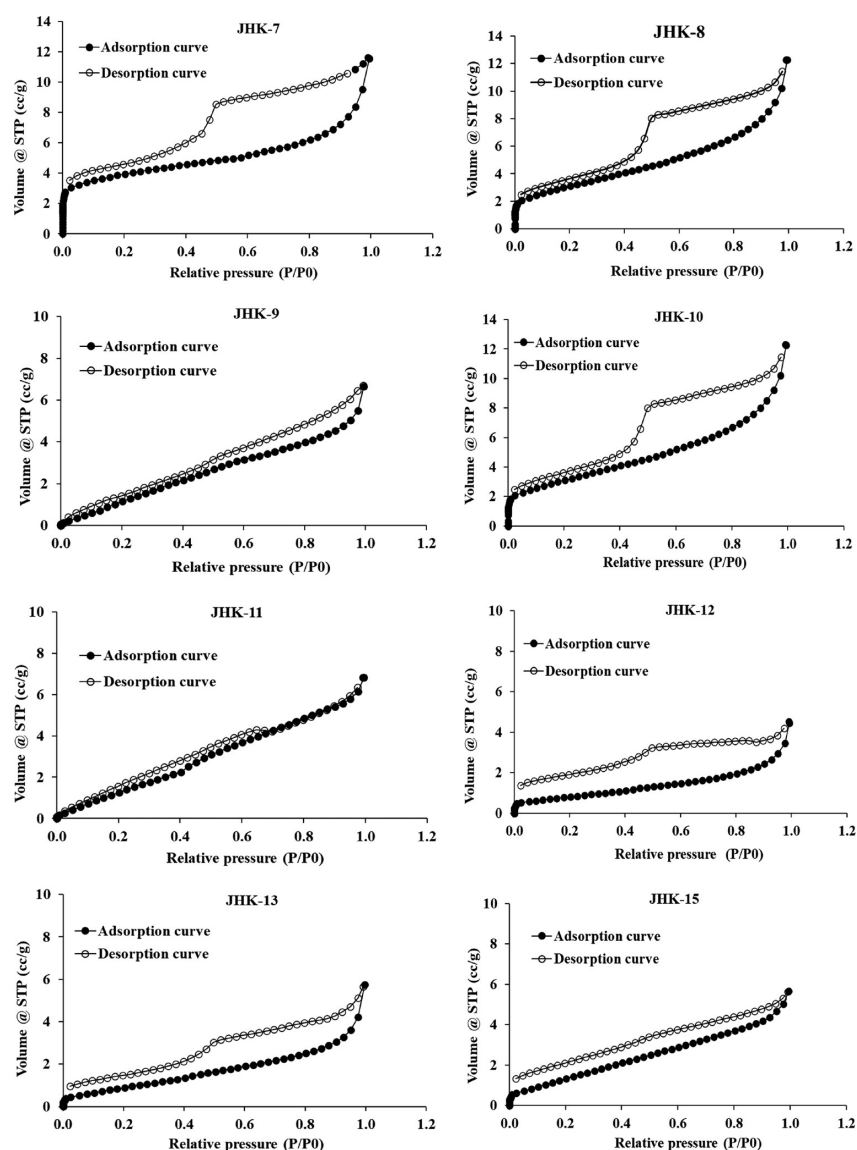


**Figure 7.** Adsorption and desorption curve showing variation in the hysteresis pattern due to different pore structures in Barakar shale samples.

A-factor (aliphatic/aromatic groups) =  $(2940 + 2850) \text{ cm}^{-1} / (2940 + 2850 + 1604) \text{ cm}^{-1}$ .

C-factor (carboxyl and carbonyl/aromatic groups) =  $1740 \text{ cm}^{-1} / (1740 + 1604) \text{ cm}^{-1}$ .

Similarly, the aliphaticity index (IAL) and the aromaticity index (IAR) are calculated using the distinct  $\text{CH}_2$  and  $\text{CH}_3$  stretching peaks as given in eqs 1 and 2.

$$\text{IAL} = \frac{(2950 + 2940 + 2850) \text{ cm}^{-1}}{(3050 + 2950 + 2940 + 2850 + 1604) \text{ cm}^{-1}} \quad (1)$$

$$\text{IAR} = \frac{(3100 + 1600) \text{ cm}^{-1}}{(3100 + 3000 + 2850 + 2800 + 1600) \text{ cm}^{-1}} \quad (2)$$

The values of the A-factor, C-factor, IAL, and IAR indicate a very narrow range due to uniform transformation of the organic content in the shales of Barakar and Barren Measures Formations (Table 2). According to ref 70, the absorption peaks of different functional groups have changed uniformly between 2800 and  $3300 \text{ cm}^{-1}$ , revealing continuous reduction in aliphatic compounds

(during transformation of kerogen I and II to III and IV), a general phenomenon obtained in matured carbon-rich shale or coal. Thus, the IAL and IAR values of the studied shales can ascertain the relative abundance of aliphaticity and aromaticity over the total aliphatics and aromatics.<sup>71,72</sup> The relation of IAL and IAR with the TOC content indicates the hydrocarbon generation trend in the studied shale (Figure 4a,b). There is a very minute difference in the Barakar and Barren Measures shale hydrocarbon genesis patterns when converting aliphatic to aromatic rings. However, the slightly higher expulsion of the aliphatic in the Barakar shale can be attributed to greater thermal maturity, which improved the relative aromaticity. The relation of A-factor and B-factor derived from the FTIR analysis of shale shows mainly type III/IV kerogen (Figure 5). It is interpreted that the organic matter of both shale formations significantly transformed and achieved moderate to matured thermal maturity.

**3.2. Sorption Pattern and Pore Structures.** Low-pressure  $\text{N}_2$  adsorption and desorption curves give information on the free pore surfaces, fractals, pore openings, pore types, and pore structures present in the shale matrix.<sup>2,5,11,20,73</sup> The gas is adsorbed and stored mainly in micro- (<2 nm), meso- (2–50 nm),

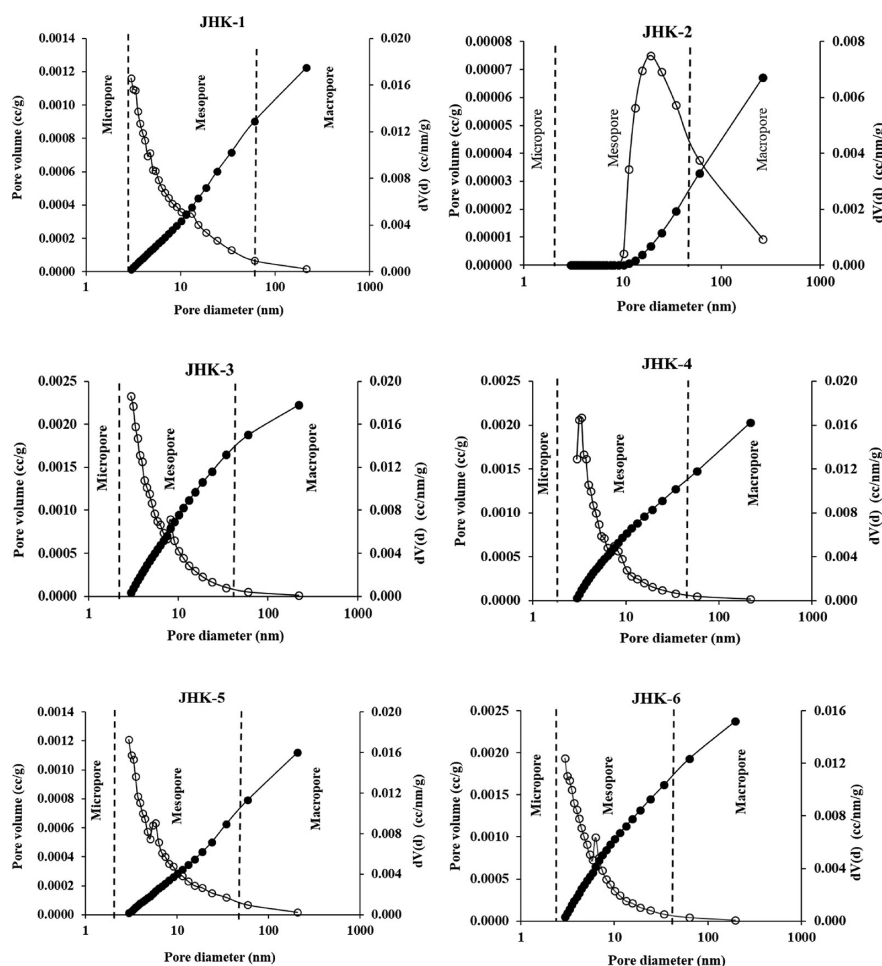


**Figure 8.** BJH plot for determination of pore size distribution and pore volume of Barren Measures shale samples.

and macropores (>50 nm). However, some of the macropores >50 nm and fracture interconnections provide a path for the gas to flow and seep into the shale. The adsorption pattern indicates the type II isotherm with desorption hysteresis of H2 and H3 (Figures 6 and 7). The likely cause for the hysteresis pattern was that capillary condensation happened in the major pores, signifying that the shale samples have abundant mesopores of slit and cylindrical structures.<sup>3,4,74</sup> The larger loop of the adsorption and desorption hysteresis pattern indicates a cylindrical pore with a slit type of opening. The unusual sorption pattern of the sample JHK-2 has mesopores mainly >10 nm, as shown in BJH plots in Figure 8. The negative adsorption in shale is due to the narrow and blind opening micropores that are difficult to admit N<sub>2</sub> gas, bearing low kinetic energy of adsorption between relative pressure ( $P/P_0$ ) range 0.2 and 1.0. In JHK-12, JHK-13, and JHK-15, open curves of adsorption and desorption indicate that the hysteresis phenomenon in low-temperature N<sub>2</sub> adsorption isotherms is usually associated with capillary condensation in mesopore structures. Generally, different shapes of hysteresis loops are caused by different types of adsorbents. Moreover, swelling/shrinking of the sample due to interaction with N<sub>2</sub> can result in low-pressure hysteresis. The pore types are classified into four categories taking into account the pore structures and openings, such as (i) cylindrical, (ii) slit, (iii) combined, and (iv) condensate (Table 3). The shale samples of Barren Measures having cylindrical (samples JHK-1, JHK-3, JHK-4, JHK-5, and JHK-6) and condensate (sample JHK-2) pores are suitable for gas adsorption and release. However, the shale belonging to

the Barakar Formation has cylindrical (samples JHK-7, JHK-8, JHK-9, and JHK-10), slit (samples JHK-13 and JHK-15), combined (samples JHK-11), and condensate (sample JHK-15) pores due to the comparatively complex geochemical properties. Barakar shale has these properties because it is older and has passed through a higher degree of thermal maturity than the Barren Measures shale, as discussed in section 3.1. Further, the desorption pattern presents a downward modulation point between the relative pressure ( $P/P_0$ ) range of 0.4 and 0.6, suggesting that a significant quantity of adsorbed gas may be released into the free wide space condensate pore structure (Figures 6 and 7). The combined pores replicate the interconnectivity of pores attributed to the organo-inorganic content (maceral and clay/mineral pore interaction) due to geochemical alterations.<sup>75</sup> The minute variation in the surface area indicated by single-point BET and multipoint BET ranges from 1.38 to 13.38 and 1.38 to 13.95 m<sup>2</sup>/g, respectively, for Barren Measures and from 3.38 to 10.91 and 3.75 to 11.26 m<sup>2</sup>/g for the Barakar shale, respectively, demonstrating the similar influence of volatile and moisture contents on rugged (fractal) surfaces of pores (Table 3). The comparatively low surface area in Barakar shale pores specifies the abundance of aromatic ring numbers associated with the aromatic series comprising the narrow pore openings and condensate structures due to the higher degree of thermal maturation. Likewise, the surface area was also determined using methods and processes such as Langmuir, BJH, DH, t-method, DR, and DFT (Table 3). The DFT method is always considered a reliable method for determining the surface area, pore size, and pore

**Table 3. Low-Pressure N<sub>2</sub> Adsorption Isotherm Type, Hysteresis Pattern, Pore Structures, and Results of Surface Area Derived from Different Methods**

sample no.	surface area (m <sup>2</sup> /g)									adsorption isotherm type	hysteresis pattern	pore structures	pore types
	single-point BET	multipoint BET	Langmuir	BJH	DH	t-method external	t-method micropore	DR	DFT				
JHK-1	13.38	13.95	22.6	7.32	7.40	9.95	4.00	38.99	10.19	type II	H1	open-end cylinder	cylindrical
JHK-2	7.97	8.24	13.24	4.81	4.86	8.24		25.72	6.66	type II	H2	open condensate	cylindrical-slit wide openings
JHK-3	12.97	13.3	20.11	3.67	3.71	6.53	6.77	23.30	13.05	type II	H1	open-end cylinder	cylindrical
JHK-4	1.38	1.38	2.75	0.34	0.38	0.57	0.81	2.61	0.67	type II	H1	open-end cylinder	cylindrical
JHK-5	1.53	2.60	2.10	0.48	0.51	1.40	1.20	0.08	3.46	type II	H1	open-end cylinder	cylindrical
JHK-6	2.88	3.07	4.87	2.03	2.06	3.07		6.30	3.96	type II	H1	open-end cylinder	cylindrical
JHK-7	8.93	9.15	14.49	4.36	4.40	3.73	1.42	25.64	8.20	type II	H1	open-end cylinder	cylindrical
JHK-8	6.29	6.53	10.83	3.10	3.13	5.64	0.88	6.46	5.22	type II	H1	open-end cylinder	cylindrical
JHK-9	8.92	9.35	16.14	5.18	5.23	7.10	2.25	8.96	8.22	type II	H2	open-interconnected	slit
JHK-10	5.09	9.11	47.41	4.89	4.95	5.13	3.98	19.02	3.61	type II	H1	open-end cylinder	cylindrical
JHK-11	7.25	8.59	2.04	6.02	6.09	8.18	0.41	2.64	5.22	type II	H1	combined interconnected	combined pores
JHK-12	8.17	9.29	19.54	6.04	6.10	8.14	1.15	27.94	5.90	type II	H2	open end—slit	large condensate pore
JHK-13	3.38	3.75	6.69	2.94	2.97	3.75		12.52	3.40	type II	H2	open end—slit	medium condensate pore
JHK-14	5.38	7.98	24.35	6.59	6.66	5.88	2.10	22.68	3.84	type II	H1	combined interconnected	combined pores
JHK-15	10.91	11.26	18.05	5.98	6.04	8.53	2.73	21.98	9.48	type II	H2	open-interconnected	slit

**Table 4. Results of Pore Size and Pore Volume Determined Using Different Methods from Low-Pressure N<sub>2</sub> Adsorption Isotherms**

sample no.	pore size (nm)						pore volume (cc/g)					
	avg.	BJH	DH	DR	DA	DFT	BET	BJH	DH	t-method	DR	DFT
JHK-1	8.69	2.98	2.98	11.68	2.90	3.97	0.022	0.018	0.017	0.002	0.014	0.019
JHK-2	9.46	2.99	2.99	12.88	3.14	3.97	0.019	0.017	0.017		0.009	0.016
JHK-3	7.38	5.09	5.09	1.82	1.68	3.97	0.018	0.013	0.012	0.003	0.008	0.016
JHK-4	4.27	3.16	3.16	6.21	2.10	1.41	0.002	0.002	0.002			0.001
JHK-5	9.46	19.22	2.99	3.14	1.38	0.78	0.017	0.006	0.006			0.004
JHK-6	8.97	3.53	3.53	2.36	1.98	1.41	0.007	0.006	0.006		0.002	0.006
JHK-7	8.17	2.99	2.99	11.89	2.98	3.97	0.019	0.016	0.016		0.009	0.016
JHK-8	8.13	3.16	3.16	1.66	1.70	3.97	0.008	0.011	0.011		0.002	0.011
JHK-9	6.77	2.99	2.99	1.70	1.68	3.97	0.016	0.013	0.013	0.001	0.003	0.014
JHK-10	4.52	2.98	2.98	12.56	3.00	3.17	0.006	0.009	0.009		0.007	0.009
JHK-11	8.12	3.33	3.33	13.12	3.12	3.97	0.017	0.016	0.015		0.009	0.014
JHK-12	7.26	2.99	2.99	12.76	3.06	3.97	0.017	0.015	0.015		0.009	0.014
JHK-13	5.48	3.34	3.34	13.29	3.16	3.80	0.008	0.004	0.008		0.004	0.007
JHK-14	5.26	3.32	3.32	13.37	3.08	2.77	0.010	0.010	0.010		0.008	0.009
JHK-15	6.74	2.99	2.99	2.09	1.84	3.97	0.019	0.016	0.015	0.001	0.007	0.016

volume of the shale samples. The average surface area determined by DFT varies from 0.67 to 13.05 and 3.40 to 9.48 m<sup>2</sup>/g for Barren Measures and Barakar shale, respectively. Hence, it is concluded that shale beds of Jharia have heterogeneous complex pore structures, a rough surface, and a sorption mechanism controlled by weathering/alteration, depositional conditions, and organo-inorganic content.<sup>91</sup>

**3.3. Evaluation of Pore Size and Its Distribution.** The pore size distribution and pore volume were determined from N<sub>2</sub> adsorption data following BJH and DFT methods (Table 4) according to the pore classification suggested by ref 76. The BJH curves show pore size distribution and cumulative pore volume, mainly the presence of mesopores in Barren Measures and Barakar shales, the nontraceable micropores, and a small



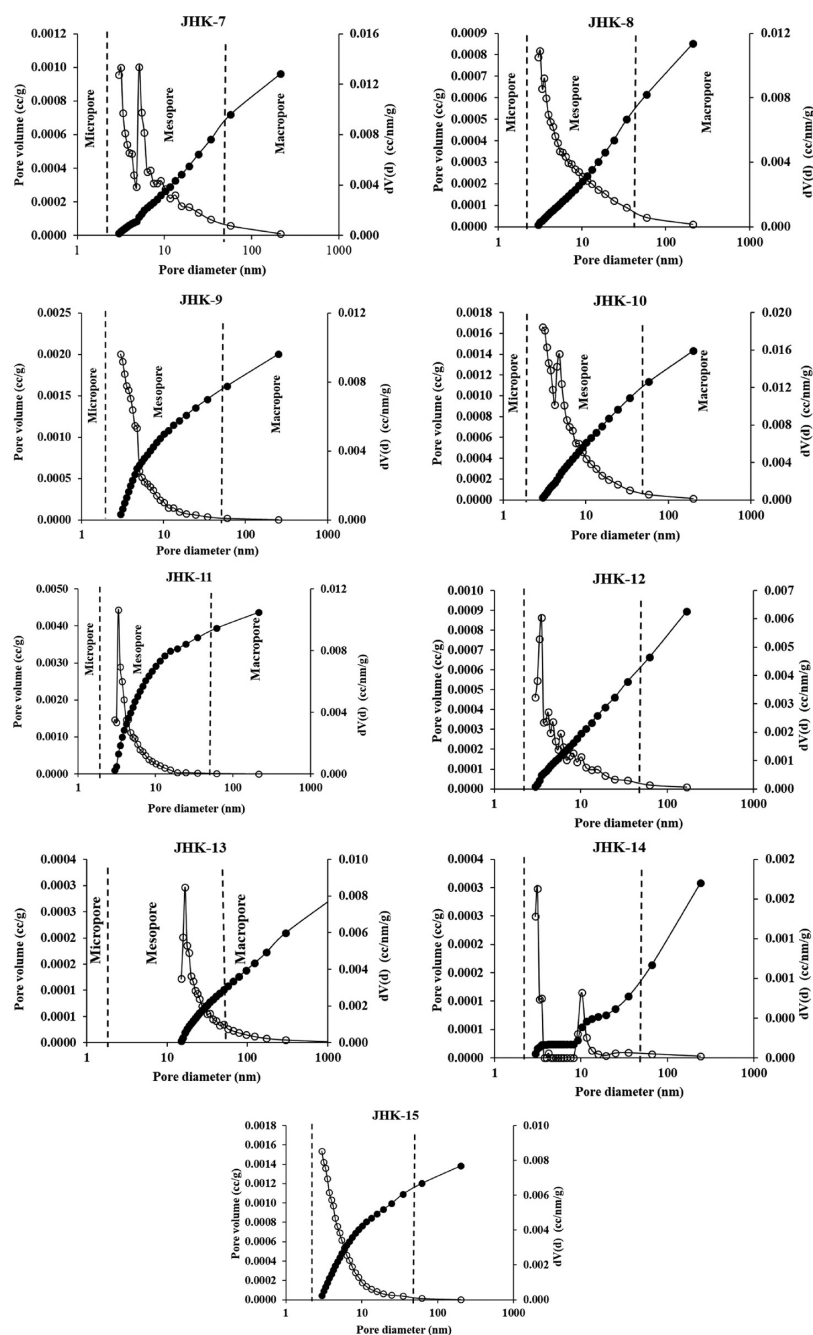


Figure 9. BJH plot for determination of pore size distribution and pore volume of Barakar shale samples.

quantity of macropores (Figures 8 and 9). The average pore sizes are determined to be 5.38–9.46 and 4.52–8.17 nm for Barren Measures and Barakar Formation shales, respectively. In DFT plots, the major part of the pore volume in Barren Measures shale is attributed to mesopores having a diameter between 2.00 and 6.00 nm. However, the Barakar shale also has a comparatively larger size mesopore distribution between 2.00 and 8.00 nm, except for shale sample JHK-13, which has a relatively more significant variation in pore distribution due to its sandy characteristics (Figures 10 and 11). According to pore abundance, the studied shale ensures that the successive trend is mesopores > macropores > micropores. Also, the DFT curves' trimodular pattern and the pore surface area concerning pore size contributed similarly to the pore volume.<sup>4,77</sup> Moreover, the variation in pore size indicates the increase in pore volume with a

decrease in pore size distribution in the shale, which suggests that the adsorption capacity in shale is highly related to the pore size difference, openings, and their structures.<sup>89,90</sup> In general, it is recorded that pores of small size have a large pore volume with a greater adsorption capacity.<sup>78</sup>

The pores observed from SEM photographs compared with the low-pressure  $N_2$  sorption pattern validate the presence of cylindrical, combined, pore-pipes, and slit pores in shale (Figure 12) such as JHK-1: large open cylindrical pores, JHK-10: combined fractured pores, JHK-11: deep rounded pore-pipes, and JHK-13: wide spacing slit pores. These pores associated with organic matter, clay, and silt are formed from the framework of organo-inorganic content and microfractures. Hence, the microfractures have a higher complexity due to the heterogeneity attributed to the banded nature of the shale. Therefore, it is summarized that Barren Measures and

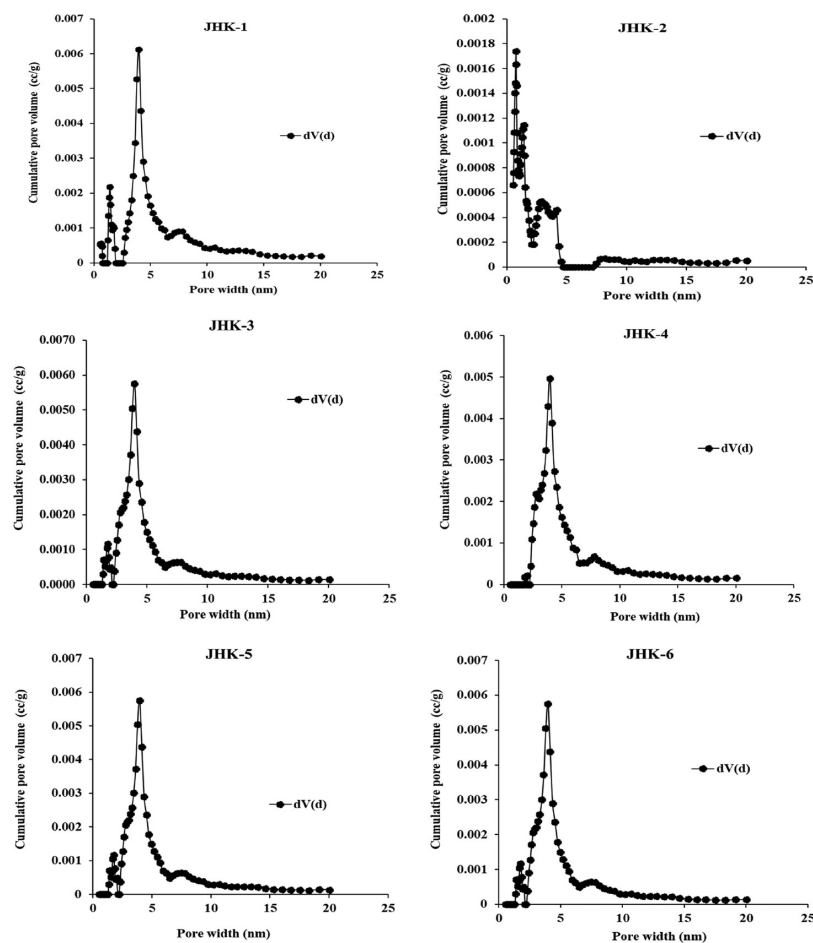


Figure 10. DFT plot for determination of pore size distribution of Barren Measures shale samples.

Barakar shale have a complex pore morphology and a narrow variation in pore size that vary from nanometers to micrometers and may significantly influence the gas storage and fluid flow mechanism in the shale.

**3.4. Types of Fractal Dimensions.** Identifying the type of fractal pore surfaces in the shale matrix system helps characterize the complex structures and gas storage capacity. Different researchers propose several models to determine pore fractal dimensions based on gas adsorption and desorption patterns like the BET model, the Langmuir model, the FHH model, and the thermodynamic model. In this study, the FHH model has been used to determine the fractal characteristics of shale pores, which can be expressed as eq 3

$$\ln \frac{V}{V_0} = A \left( \ln \left( \ln \left( \frac{P_0}{P} \right) \right) \right) + \text{constant} \quad (3)$$

where  $V$  is the adsorbed gas volume,  $V_0$  is the monolayer adsorbed gas volume,  $P$  is the equilibrium pressure,  $P_0$  is the saturated vapor pressure of gas, and  $A$  is the slope depending on the adsorption pattern and pore fractals. Thus, the values of fractal dimensions ( $D$ ) can be calculated using eqs 4 or 5

$$D = A + 3 \quad (4)$$

or

$$D = 3A + 3 \quad (5)$$

The equation  $D = A + 3$  was applied for the hollow portion in shale pores shown by hysteresis loops initiating capillary condensation;

however, the equation  $D = 3A + 3$  applies to the van der Waals force.<sup>5,79,88</sup> The  $\ln(V)$  vs  $\ln[\ln(P_0/P)]$  plots of Barren Measures and Barakar shale samples displaying three distinct fractal dimension surfaces corresponding to micro-, meso-, and macropores are shown in Figures 13 and 14. The fractal dimension  $D_1$  was calculated from linear sections at  $P/P_0$  between 0.0002 and 0.0090,  $D_2$  was calculated from linear sections at  $P/P_0$  between 0.0090 and 0.3000, and  $D_3$  was estimated from the linear sections at  $P/P_0$  between 0.3000 and 1.0000. The fractal fitting equations and fractal dimension values for the studied shale samples are given in Tables 4 and 5, respectively. The values of  $D_1$ ,  $D_2$ , and  $D_3$  of the Barren Measures shale are in the range of 1.25–2.17, 2.09–2.55, and 2.57–2.76, respectively, while the Barakar shale fractal values varying in the range of 1.45–2.09, 1.11–2.53, and 2.69–2.76, respectively (Table 6). The correlation coefficient of fractal fitting equations ( $R_2^2$  and  $R_3^2$ ) of  $D_2$  and  $D_3$  is greater than 0.95, indicating Barren Measures and Barakar shale pore systems with noticeable fractal surfaces mostly from meso- and macropores. However, it is interpreted that both the formation shales have composite pore internal structures attributed to three different kinds of fractals. The Barakar shale with a comparatively higher thermal maturity developed more irregular pore surfaces during dehydration and devolatilization. It results in the amalgamation of complex macropores to mesopores (Figure 14). Also, the fractal surfaces amplified with increasing  $P/P_0$ , specifying that compared with the bigger pores (macropores), the smaller pores (micro- and mesopores) are more complex and composite. The  $D_2$  and  $D_3$

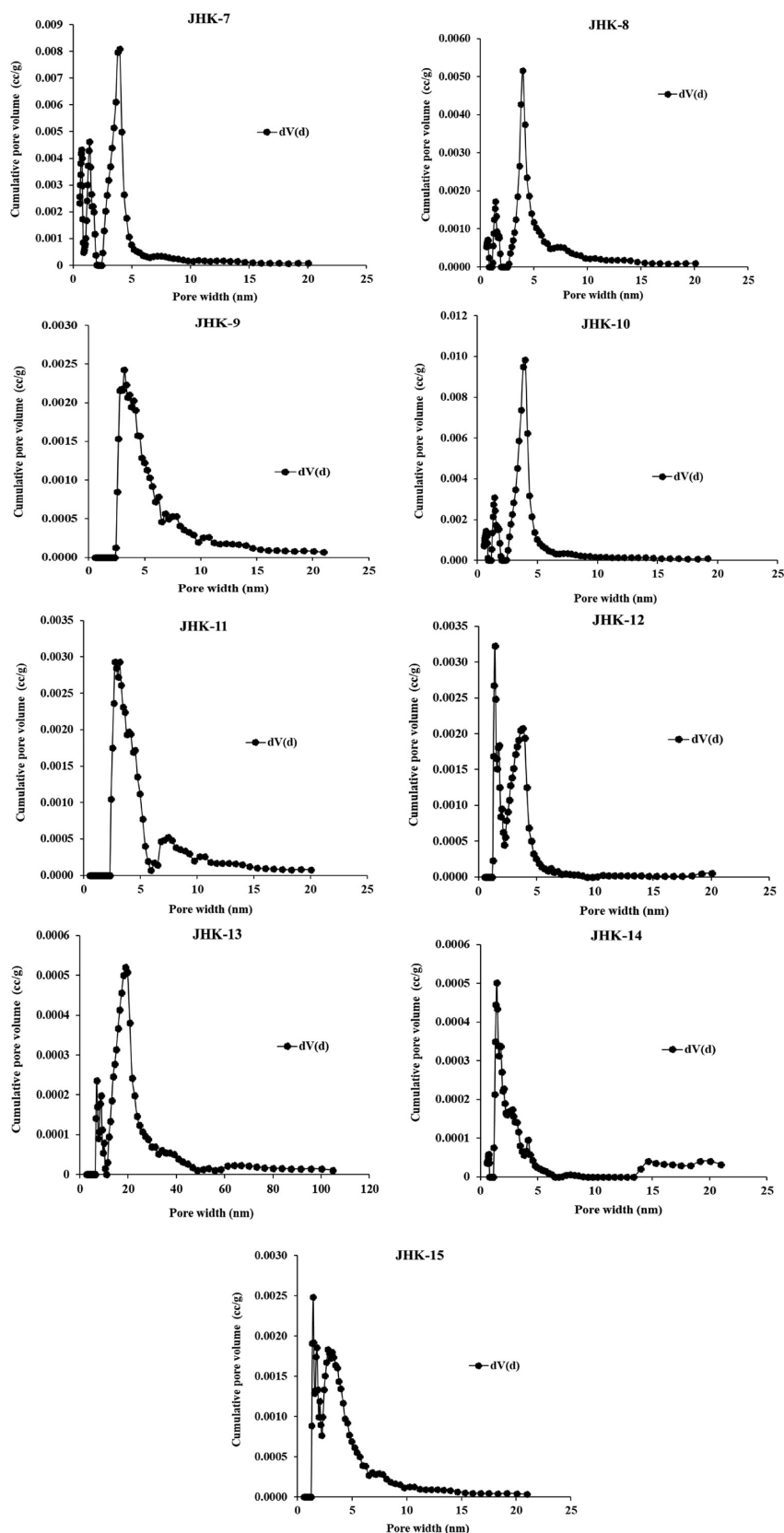
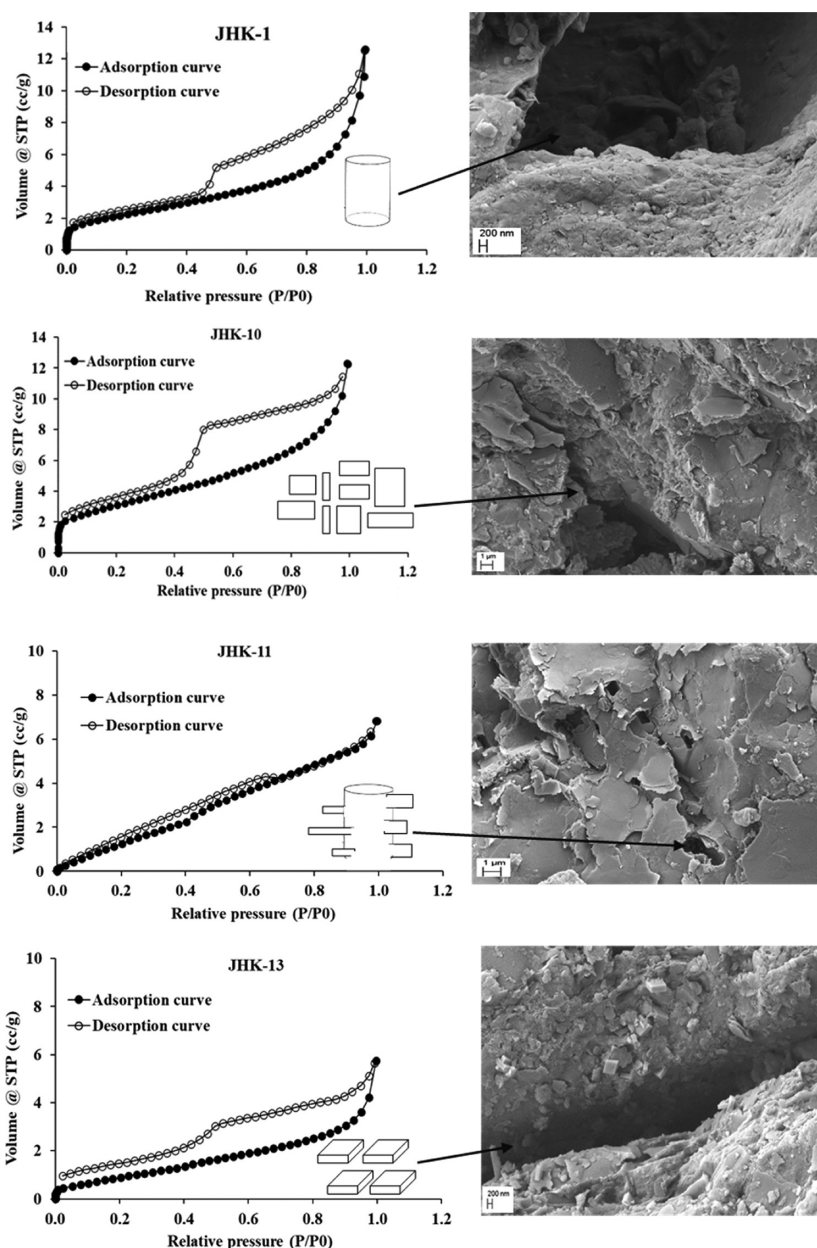


Figure 11. DFT plot for determination of pore size distribution of Barakar shale samples.

represent the meso- and macropores with a fractal value near 3. Mainly, the intergranular pores that occur between grains of organic and inorganic contents dominate the meso- and macropores. However, the organic pores, kaolinite fissility openings

along the bedding planes, and the subrounded to rounded spacing in grains of quartz, feldspar, and carbonate minerals also contribute to the meso- and macropores. Numerous researchers have stated that the clay mineral content is an important factor



**Figure 12.** Low-pressure  $N_2$  sorption isotherms showing the presence of different types of pores validated by SEM photographs.

influencing the shale pore structure; hence, the clay mineral also contributes to the fractal dimension.<sup>5,15,80,88</sup>

**3.5. Relationship of Fractal Dimensions with Shale Properties.** The different properties of shale directly influence fractal pore surfaces.<sup>5,11,79,88</sup> The fractal dimensions  $D_1$ ,  $D_2$ , and  $D_3$  show successive transitions due to change in thermal maturity (Figure 15a,c). The release of volatiles due to the cracking of hydrocarbon compound of shale matrix leads to the formation of rugged pore surfaces. A similar trend shown by the relation of fractals with fixed carbon specify succeeding carbon enrichment due to thermal transformation of organic matter contributed to the rough pore surfaces (Figure 15b,e). The TOC content influences the advancement of pores in shales. More pores evolved in higher TOC content shales, and the complex pore surfaces and structures led to greater fractal dimensions. Earlier investigations had shown that the clay and mineral content are a vital aspect controlling the pore types and pore structure of shale.<sup>5,15,80,81</sup> The increasing trend of fractal dimension with the

ash content of shale demonstrates that inorganic content also contributed to the formation of pore surfaces (Figure 15d). The rounded to subrounded grains of minerals (e.g., quartz, feldspar, etc.) associated with clays shaped pore surfaces. The variation in fractal dimensions ( $D_1$ ,  $D_2$ , and  $D_3$ ) with depth indicates that heterogeneity in lithotype, organo-inorganic content, and thermal maturity controls the construction anomaly of fractal surfaces (Figure 15f).

**3.6. Empirical Model for Estimation of Porosity and Permeability.** The measurement of porosity and permeability of shale is time-consuming and expensive. Therefore, an empirical method is formulated and proposed to estimate porosity and permeability considering the fractal dimensions, pore size, and pore volume considering their constructive and adverse influences. The relations of measured porosity (MPOc) and measured permeability (MPEc) were evaluated with fractal dimensions, pore size, and pore volume. The moderate linear relationship of MPOc with MPEc ( $R^2 = 0.4165$ ) indicates pore



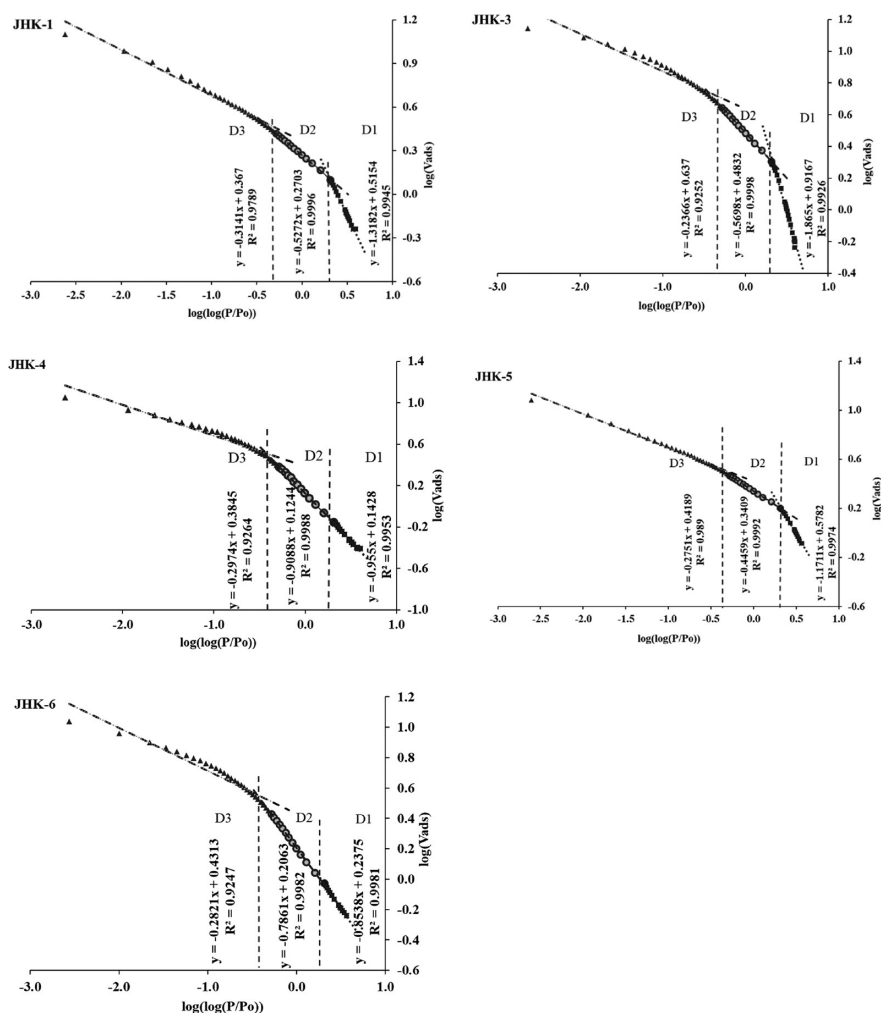


**Figure 13.** Presence of three distinct fractal dimensions derived by the FHH method for Barren Measure shale samples showing region I ( $P/P_0 = 0.0002–0.0090$ ;  $D_1$ ), region II ( $P/P_0 = 0.0090–0.3000$ ;  $D_2$ ), and region III ( $P/P_0 = 0.3000–1.0$ ).

connectivity suitable for gas flow in a shale (Figure 16a). The  $D_1$  showed a negligible relationship with MPOc, emphasizing that plane surfaces seldom contribute to porosity in shales (Figure 16b). However, the very good linear relation of  $D_2$  ( $R^2 = 0.8442$ ) and  $D_3$  ( $R^2 = 0.6809$ ) with MPOc (Figure 16c,d) specifies that these fractals are mainly remunerating the porosity in shale through the active rough surfaces of pores formed by the heterogeneous content of organo-inorganic matter.

Similarly, fractals  $D_2$  and  $D_3$  also showed a direct moderate correlation with MPEc, indicating the combined effects of rugged surfaces on the gas flow mechanism in the pore-associated matrix system of the shale (Figure 16f,g). The poor relation of  $D_1$  fractal with MPEc suggests that smooth surfaces have a trivial influence on permeability due to low affinity (Figure 16e). The moderate positive relationship of average pore size and MPEc illustrates that the larger pore opening supports the gas flow because of low turbulence and low capillary pressure (Figure 16h). The MOPc and MPEc showed a linear moderate to very good relation with the BET pore volume ( $R^2 = 0.5213$  and  $0.8422$ ), signifying that matrix containing pores are mainly interconnected (Figure 16i,j) and interdependent. However, the maceral, mineral, and clays have different porous features due to intricacy in their chemical composition; pore size variation led to fractal dimensions appropriate for adsorption, storage, and flow of gas in shales.<sup>82,83</sup>

Considering the significance of the above-explained parameters, the following empirical equation is drawn to estimate porosity and permeability in shale<sup>5,11</sup>

$$\begin{aligned} & \text{estimated porosity (EPO}_f) \\ &= \left( \left( \frac{(0.2 \times PV_{\text{BET}} + D_2 + D_3)}{(4.0 - 0.2 \times D_3 - 0.7 \times D_2)} \right) \div 100 \right) \times 100 \\ & - 1.3 \end{aligned} \quad (6)$$

where  $\text{EPO}_f$  is the estimated porosity by an empirical method using pore fractals,  $PV_{\text{BET}}$  is the pore volume determined by the BET method, and  $D_2$  and  $D_3$  are fractal dimensions.

$$\begin{aligned} & \text{estimated permeability (EPE}_f) \\ &= \left( \frac{(0.3 \times PV_{\text{BET}})}{0.2 \times (PS_A + 0.5 \times D_3 + 5.8 \times D_2 + 0.5 \times D_1)} \right) \end{aligned} \quad (7)$$

where  $\text{EPE}_f$  is the estimated permeability by the empirical method using pore fractals,  $PV_{\text{BET}}$  is the pore volume determined by the BET method,  $D_1$ ,  $D_2$ , and  $D_3$  are fractal dimensions, and  $PS_A$  is the average pore size.

The estimated porosity ( $\text{EPO}_f$ ) and permeability ( $\text{EPE}_f$ ) derived from the suggested empirical formula (Table 7) vary

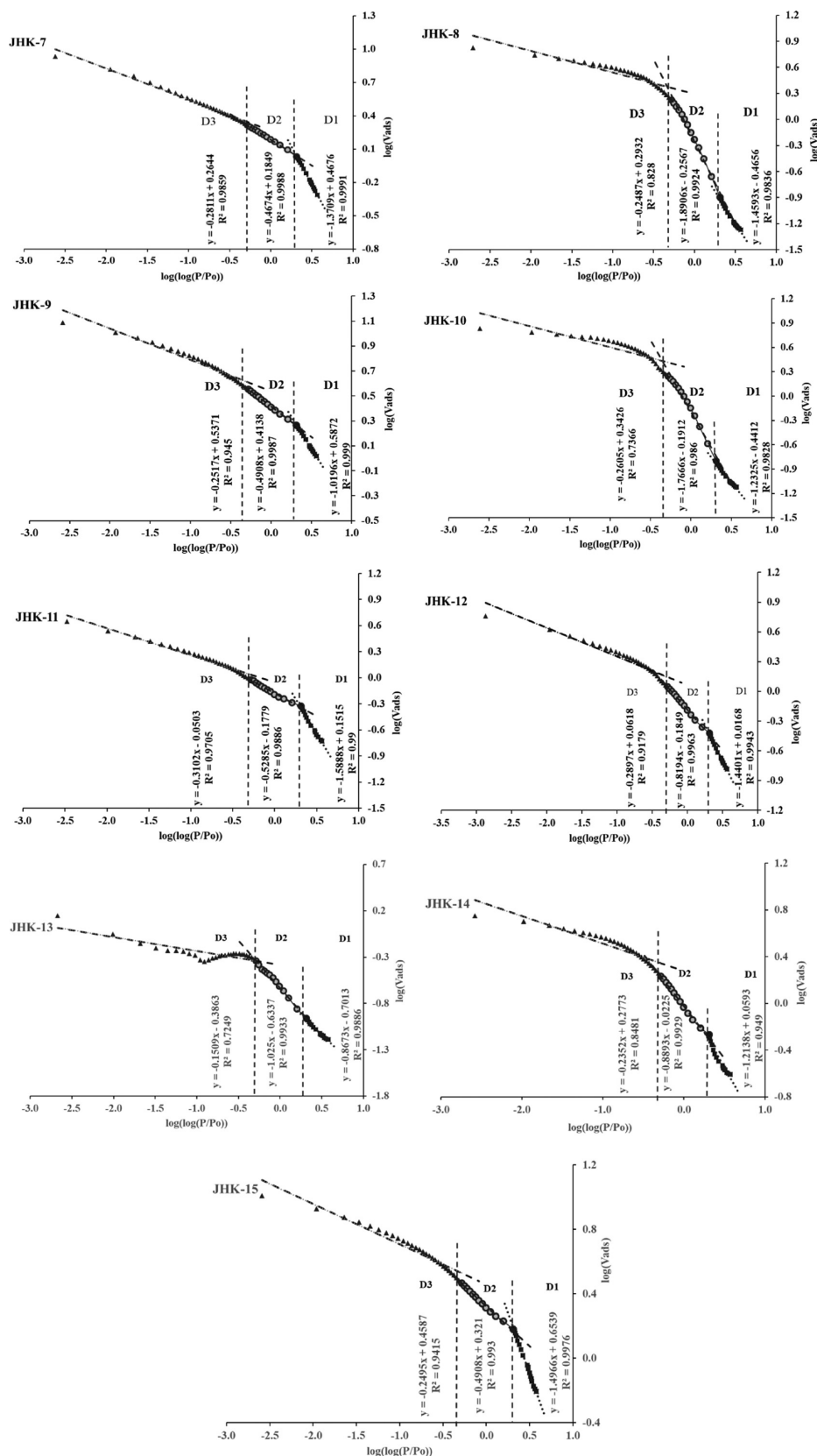


**Figure 14.** Presence of three distinct fractal dimensions derived by the FHH method for Barakar shale samples region I ( $P/P_0 = 0.0002\text{--}0.0090$ ;  $D_1$ ), region II ( $P/P_0 = 0.0090\text{--}0.3000$ ;  $D_2$ ), and region III ( $P/P_0 = 0.3000\text{--}1.0$ ).

from 0.98 to 1.58% and 0.35 to 0.63 mD for Barren Measures; however, for Barakar Formations, it is estimated to be 0.75–1.65% and 0.41–0.62 mD, respectively. The estimated values of

porosity ( $EPO_f$ ) and permeability ( $EPE_f$ ) showed an excellent linear correlation with the measured porosity ( $MPO_c$ ,  $R^2 = 0.8577$ ) and permeability ( $MPE_c$ ,  $R^2 = 0.8577$ ), which are close

Table 5. Fractal Fitting Equations for the Studied Shale Core Samples

sample no.	region I ( $P/P_0 = 0.0002-0.0090; D_1$ )		region II ( $P/P_0 = 0.0090-0.3000; D_2$ )		region III ( $P/P_0 = 0.3000-1.0000; D_3$ )	
	fractal fitting equation	fitting coefficient	fractal fitting equation	fitting coefficient	fractal fitting equation	fitting coefficient
JHK-1	$y = -1.3182x + 0.5154$	0.9945	$y = -0.5272x + 0.2703$	0.9996	$y = -0.3141x + 0.367$	0.9789
JHK-2	$y = -1.512x + 0.6154$	0.9921	$y = -0.4836x + 0.3075$	0.9845	$y = -0.3602x + 0.463$	0.9208
JHK-3	$y = -1.865x + 0.9167$	0.9926	$y = -0.5698x + 0.4832$	0.9998	$y = -0.2366x + 0.637$	0.9252
JHK-4	$y = -0.955x + 0.1428$	0.9953	$y = -0.9088x + 0.1244$	0.9988	$y = -0.2974x + 0.3845$	0.9264
JHK-5	$y = -1.1711x + 0.5782$	0.9974	$y = -0.4459x + 0.3409$	0.9992	$y = -0.2751x + 0.4189$	0.9890
JHK-6	$y = -0.8538x + 0.2375$	0.9981	$y = -0.7861x + 0.2063$	0.9982	$y = -0.2821x + 0.4313$	0.9247
JHK-7	$y = -1.3709x + 0.4676$	0.9991	$y = -0.4674x + 0.1849$	0.9988	$y = -0.2811x + 0.2644$	0.9859
JHK-8	$y = -1.4593x - 0.4656$	0.9836	$y = -1.8906x - 0.2567$	0.9924	$y = -0.2487x + 0.2932$	0.8280
JHK-9	$y = -1.0196x + 0.5872$	0.9990	$y = -0.4908x + 0.4138$	0.9987	$y = -0.2517x + 0.5371$	0.9450
JHK-10	$y = -1.2325x - 0.4412$	0.9828	$y = -1.7666x - 0.1912$	0.9860	$y = -0.2605x + 0.3426$	0.7366
JHK-11	$y = -1.5888x + 0.1515$	0.9900	$y = -0.5285x - 0.1779$	0.9886	$y = -0.3102x - 0.0503$	0.9705
JHK-12	$y = -1.4401x + 0.0168$	0.9943	$y = -0.8194x - 0.1849$	0.9963	$y = -0.2897x + 0.0618$	0.9179
JHK-13	$y = -0.8673x - 0.7013$	0.9886	$y = -1.025x - 0.6337$	0.9933	$y = -0.1509x - 0.3863$	0.7249
JHK-14	$y = -1.2138x + 0.0593$	0.9490	$y = -0.8893x - 0.0225$	0.9929	$y = -0.2352x + 0.2773$	0.8481
JHK-15	$y = -1.4966x + 0.6539$	0.9976	$y = -0.4908x + 0.321$	0.9930	$y = -0.2495x + 0.4587$	0.9415

Table 6. Results of Fractal Dimensions of Shale Core Samples

sample no.	region I ( $P/P_0 = 0.0002-0.0090; D_1$ )				region II ( $P/P_0 = 0.0090-0.3000; D_2$ )				region III ( $P/P_0 = 0.3000-1.0000; D_3$ )			
	$A_1$	$D_1 = 3 + A_1$	$D_1 = 3 + 3A_1$	$R_1^2$	$A_2$	$D_2 = 3 + A_2$	$D_2 = 3 + 3A_2$	$R_2^2$	$A_3$	$D_3 = 3 + A_3$	$D_3 = 3 + 3A_3$	$R_3^2$
JHK-1	-1.35	1.85	-1.05	0.99	-0.50	2.50	1.49	1.00	-0.31	2.69	2.06	0.98
JHK-2	-1.51	1.38	-1.22	0.98	-0.61	2.47	1.60	0.99	-0.35	2.72	2.14	0.97
JHK-3	-1.75	1.25	-2.24	0.99	-0.57	2.43	1.29	1.00	-0.24	2.76	2.29	0.93
JHK-4	-0.99	1.11	0.03	1.00	-0.91	1.85	0.28	1.00	-0.43	2.27	1.71	0.93
JHK-5	-1.14	1.86	-0.42	1.00	-0.45	2.55	1.66	1.00	-0.28	2.72	2.18	0.99
JHK-6	-0.83	2.07	0.52	1.00	-0.79	2.21	0.64	1.00	-0.28	2.72	2.15	0.92
JHK-7	-1.37	1.63	-1.12	1.00	-0.47	2.53	1.60	1.00	-0.28	2.72	2.16	0.99
JHK-8	-1.42	1.58	-1.27	0.98	-1.89	1.61	-2.67	0.99	-0.25	2.18	2.25	0.83
JHK-9	-1.02	1.98	-0.05	1.00	-0.49	2.51	1.53	1.00	-0.25	2.75	2.24	0.95
JHK-10	-1.20	1.80	-0.60	0.98	-1.77	1.63	-2.30	0.99	-0.26	2.44	2.22	0.74
JHK-11	-1.55	1.45	-1.64	0.99	-0.53	2.47	1.41	0.99	-0.31	2.69	2.07	0.97
JHK-12	-1.41	1.59	-1.24	0.99	-0.82	2.18	0.54	1.00	-0.29	2.71	2.13	0.92
JHK-13	-0.91	2.09	0.28	0.99	-1.01	1.99	-0.04	0.99	-0.27	2.73	2.18	0.72
JHK-14	-1.17	1.83	-0.50	0.95	-0.89	2.11	0.33	0.99	-0.24	2.76	2.30	0.85
JHK-15	-1.51	1.49	-1.53	1.00	-0.49	2.51	1.53	0.99	-0.25	2.75	2.25	0.94

to the measured values. It is concluded that the proposed empirical formula for  $EPO_f$  and  $EPE_f$  may be a suitable indirect method for the estimation of porosity and permeability of shale samples (Figure 17a,c). Further, the validation of  $EPO_f$  and  $EPE_f$  calculated values has been done through a curve match with measured porosity and permeability and are presented in Figure 17b,d. The excellent curve matching demonstrates that the proposed empirical models can be used for the estimation of porosity and permeability.

#### 4. SUMMARY AND CONCLUSIONS

The carbon-rich Barakar and Barren Measures shale beds of the Jharia basin were evaluated for organo-inorganic composition by FTIR, pore size, and pore structure using BET low-pressure  $N_2$  adsorption and pore geometry through FE-SEM photographs. The study provides insights into the variation of organo-inorganic formed pores, pore structures, surface area, and fractal dimensions regarding the gas storage and recovery mechanism from shale. The following conclusions have been drawn from the study.

- i. The shale samples have significant carbon-rich content and are intercalated-banded in nature, indicating fluviatile-lacustrine facies of deposition.

- ii. The fractal dimensions  $D_1$ ,  $D_2$ , and  $D_3$  showed successive transitions due to change in thermal maturity.
- iii. The values of A-factor, C-factor, IAL, and IAR indicate a very narrow range due to the uniform transformation of organic content in the shales of Barakar and Barren Measures Formations.
- iv. The FE-SEM images indicated shallow to deep pores with different pore structures having fair to good pore connectivity.
- v. The shale beds of Jharia have heterogeneous complex pore structures, rough surface, and sorption mechanism controlled by weathering/alteration, depositional conditions, and organo-inorganic content.
- vi. The variation in pore size indicates the increase in pore volume with a decrease in pore size distribution in the shale, which suggests that the adsorption capacity in the shale is highly related to the pore size difference, openings, and their structures.
- vii. The slightly higher expulsion of the aliphatic in Barakar shale was attributed to the greater thermal maturity, which improved the relative aromaticity.
- viii. The calculated values using proposed empirical models for porosity ( $EPO_f$ ) and permeability ( $EPE_f$ ) showed an

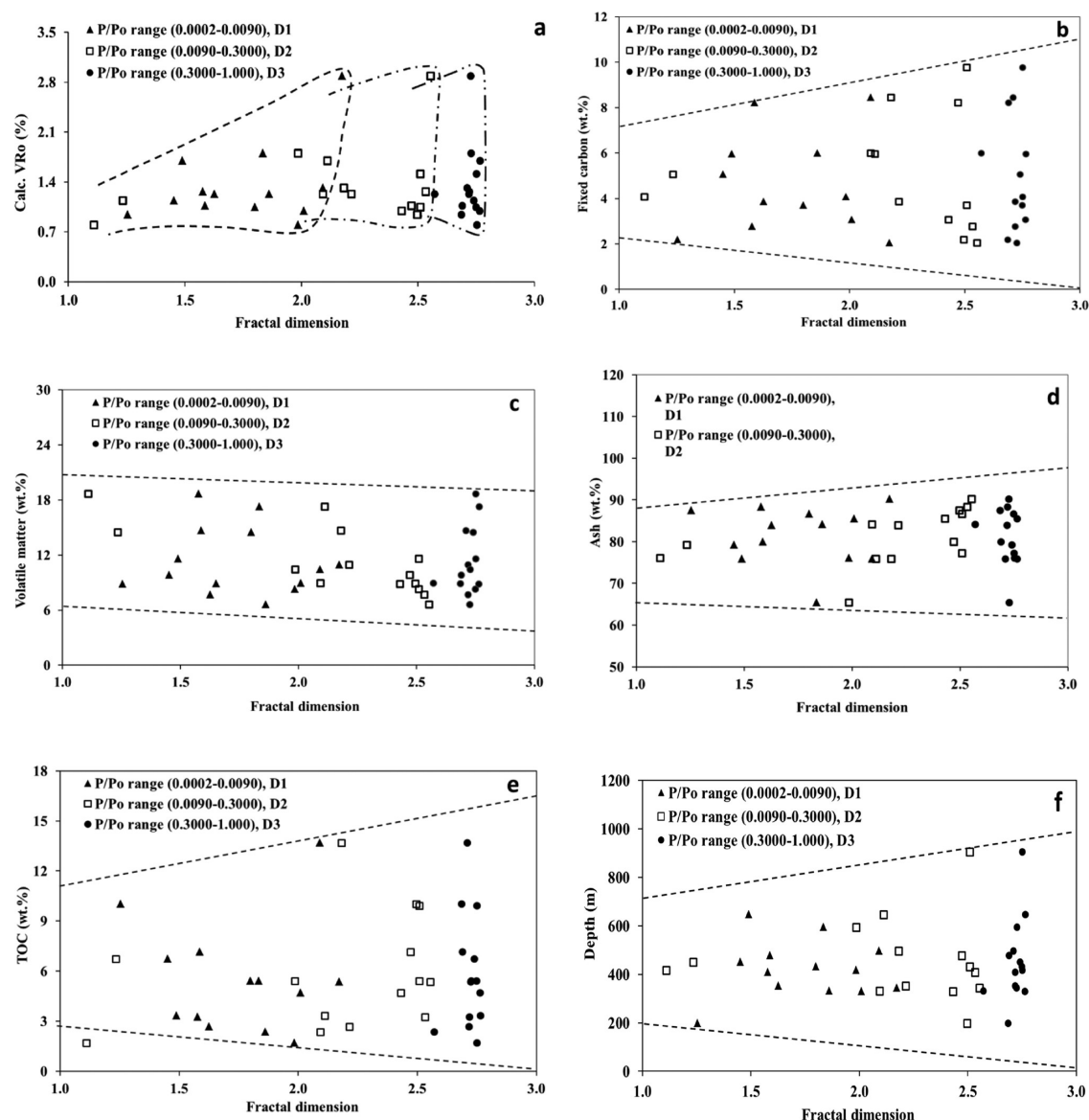


**Figure 15.** Relationship of fractal dimensions with different properties of shale, (a) fractal dimensions vs calc. VR<sub>o</sub> (thermal maturity), (b) fixed carbon vs fractal dimensions, (c) volatile matter vs fractal dimensions, (d) ash content vs fractal dimensions, (e) TOC vs fractal dimensions, and (f) depth of occurrence vs fractal dimensions.

excellent linear correlation with the measured porosity (MPOc) and permeability, which are close to measured values. The proposed models may be considered to estimate the porosity and permeability of shale and coal beds.

## 5. MATERIALS AND METHODS

**5.1. Shale Core Sampling and Preparation.** A total of 14 shale core samples were obtained from four boreholes (BH-1, BH-2, BH-3, and BH-4) drilled in the Jharia basin with laterally varying depth and thickness of the beds. The shale samples were manually crushed and sieved for further analysis like TOC, low-pressure N<sub>2</sub> sorption, and scanning electron microscopy (SEM) and in the sizes of 72 mesh (212 μm), 0.8–1.0 mm, and 1.0–2.0 mm, respectively.

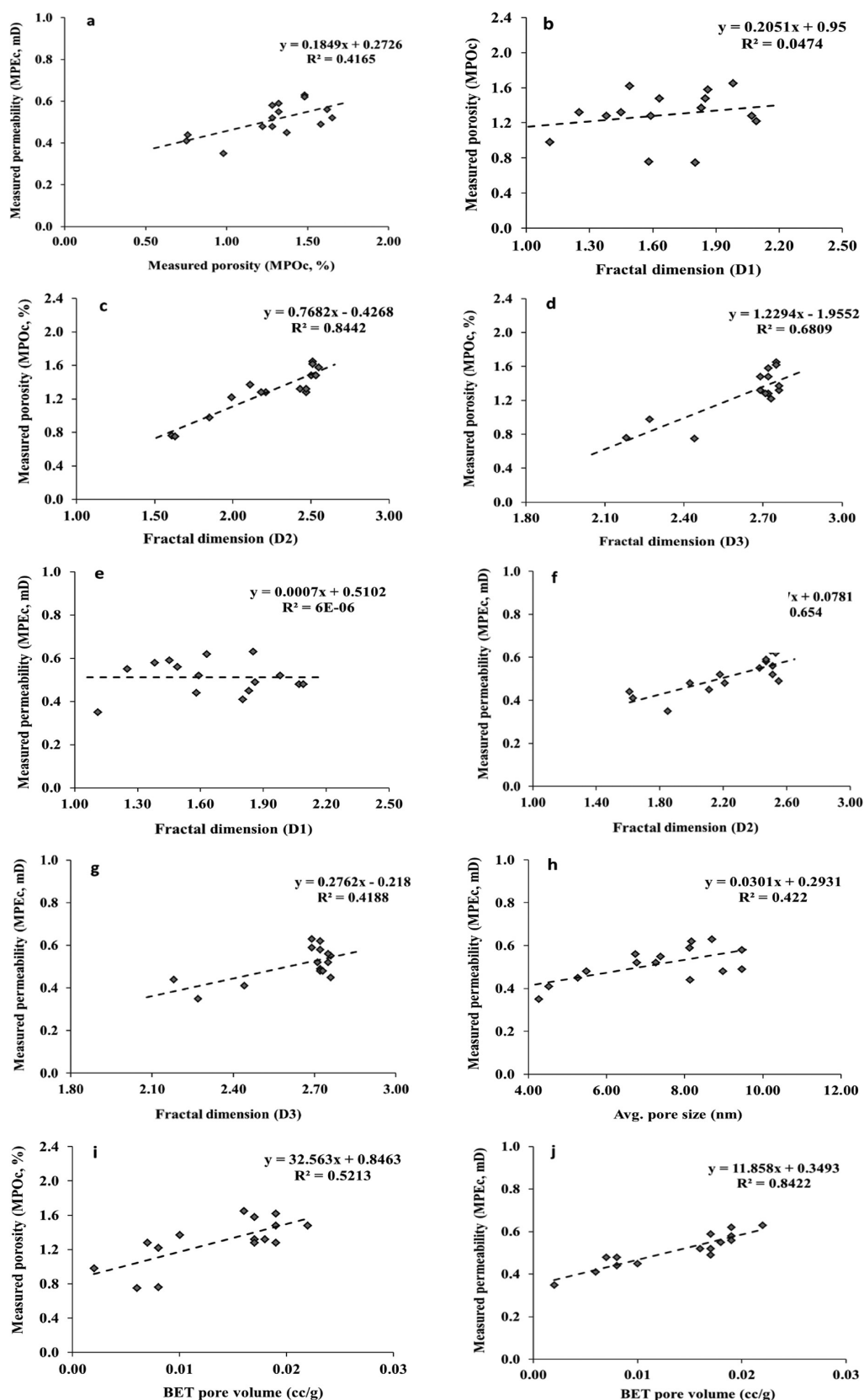
**5.2. Total Organic Carbon (TOC) Analysis.** The prepared shale samples of size 212 μm were analyzed for TOC using the Vinci Technologies “Rock-Eval 6 Plus TOC module” system.

The TOC content of the shale was measured through oxidation under air. The contents of the pyrolyzable carbon and mineral-carbon were determined by thermally disintegrating the sample using a pyrolysis oven. More details about TOC determination using the Rock-Eval 6 system have been explained by different researchers.<sup>2,7,11</sup>

**5.3. Low-Pressure N<sub>2</sub> Adsorption Isotherm.** The Quantachrome Autosorb iQ was used to measure the low-pressure N<sub>2</sub> adsorption and desorption isotherm following the Brunauer–Emmett–Teller (BET) method. The surface area, pore size, pore volume, and fractal dimensions of micro-, meso-, and macropores were determined following the procedures and models like multipoint BET, density functional theory (DFT), Langmuir, Barrett–Joyner–Halenda (BJH), *t*-test, and Frenkel–Halsey–Hill (FHH).

**5.4. FTIR Spectroscopy.** The shale samples were crushed to −75 μm, and 1 mg was mixed with 100 mg of KBr, followed by grounding the mixtures in an agate mortar pestle. The homogenized mixture was pressed in an exiled die to form pellets

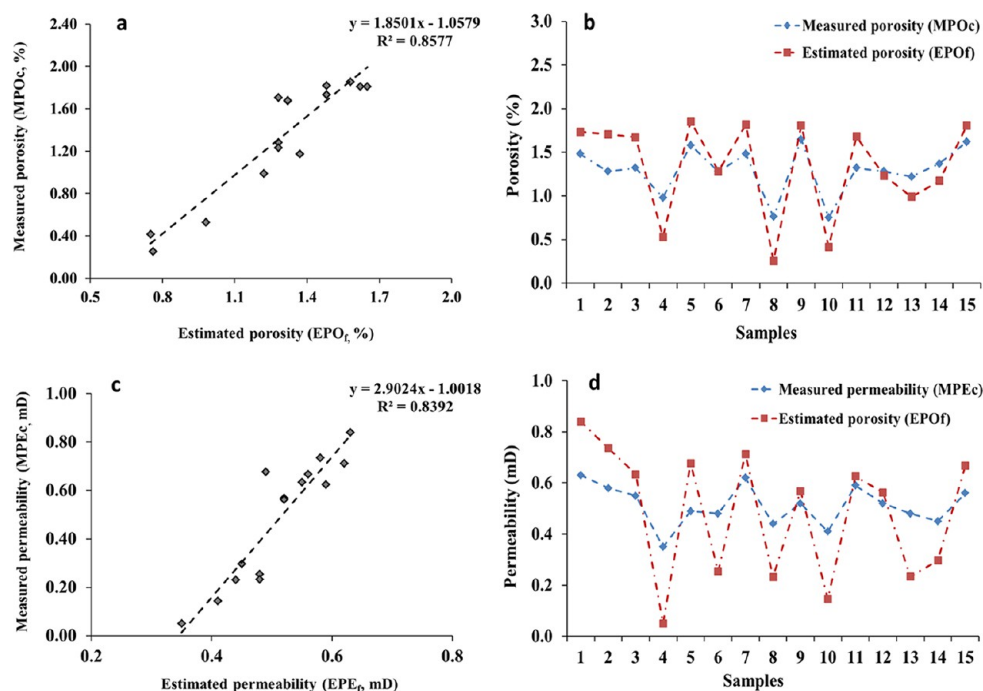




**Figure 16.** Relations of porosity and permeability with fractal dimensions, (a) porosity vs permeability, (b) fractal dimension ( $D_1$ ) vs porosity, (c) fractal dimension ( $D_2$ ) vs porosity, (d) fractal dimension ( $D_3$ ) vs porosity, (e) fractal dimension ( $D_1$ ) vs permeability, (f) fractal dimension ( $D_2$ ) vs permeability, (g) fractal dimension ( $D_3$ ) vs permeability, (h) average pore size vs permeability, (i) BET pore volume vs porosity, and (j) BET pore volume vs permeability.

**Table 7. Results of Measured Permeability and Porosity under Reservoir-Simulated Confining Pressure and Proposed Empirical Model of Shale Core Samples**

sample no.	depth (m)	measured permeability			measured porosity			estimated porosity and permeability	
		inlet pressure (psi)	confining pressure (psi)	permeability (MPE <sub>c</sub> ) (mD)	equilibrium pressure (psi)	confining pressure (psi)	porosity (MPO <sub>c</sub> ) (%)	permeability (EPE <sub>t</sub> ) (mD)	porosity (EPO <sub>t</sub> ) (%)
JHK-1	197	260.11	282.74	0.63	123.45	285.33	1.48	1.73	0.84
JHK-2	289	396.45	412.18	0.58	285.02	415.23	1.28	1.71	0.74
JHK-3	329	448.69	468.75	0.55	310.56	458.69	1.32	1.67	0.63
JHK-4	331	458.05	472.23	0.35	328.96	475.02	0.98	0.53	0.05
JHK-5	343	462.85	486.32	0.49	368.42	483.79	1.58	1.86	0.68
JHK-6	351	480.69	500.21	0.48	394.08	502.14	1.28	1.28	0.25
JHK-7	408	565.23	582.76	0.62	412.26	585.36	1.48	1.82	0.71
JHK-8	416	575.26	592.63	0.44	436.85	594.65	0.76	0.26	0.23
JHK-9	431	595.18	615.49	0.52	456.78	614.96	1.65	1.81	0.57
JHK-10	450	605.14	635.29	0.41	485.12	636.32	0.75	0.42	0.14
JHK-11	476	660.47	680.12	0.59	512.20	682.45	1.32	1.68	0.63
JHK-12	496	686.69	706.58	0.52	528.67	708.29	1.28	1.23	0.56
JHK-13	594	827.30	845.36	0.48	645.29	848.25	1.22	0.99	0.23
JHK-14	646	894.55	919.05	0.45	746.95	922.85	1.37	1.17	0.30
JHK-15	904	1270.08	1286.36	0.56	1052.52	1288.20	1.62	1.81	0.67

**Figure 17.** Validation of estimated porosity and permeability, (a) estimated porosity (EPO<sub>t</sub>) vs measured porosity (MPO<sub>c</sub>), (b) matching curve of measured and estimated porosity, (c) estimated permeability (MPE<sub>t</sub>) vs measured permeability (MPE<sub>c</sub>), and (d) matching curve of measured and estimated permeability.

following the procedure described in ref 25. Pellets were dried in a vacuum oven for 48 h to remove extra moisture and minimize their influence on FTIR spectra. FTIR analysis was conducted under a Bruker, 3000 Hyperion Microscope with a Vertex 80 FTIR system at IIT Mumbai in the wavelength range of 4000–400  $\text{cm}^{-1}$  in the absorbance mode.

**5.5. FE-SEM Analysis.** SEM is an advanced tool to study the microfeatures of shale/coal. SEM photographs were used to find out the pore morphology, pore structures, secondary mineral infillings in fracture-pores, organo-inorganic homogeneity, and cleat spacing. The Carl Zeiss-make “FE-SEM Supra 55” with an EDX attachment under magnifications ranging from

4k $\times$  to 40k $\times$  was used. We took out small chips of shale samples from the core with the help of a chisel. The chips were mounted on brass stubs using silver glue paste and coated with platinum. The photographs were taken from a focused ion beam of different magnitudes. The SEM photographs were marked with 2D surface features (e.g., pore types, openings, structures, aperture, spacings, organo-inorganic allied pores, and fractures).

**5.6. Measurement of Porosity and Permeability under Reservoir-Simulated Confining Pressure.** The porosity and permeability determination of core samples under confining pressure with accuracy is very vital to design and plan gas recovery from a shale reservoir. The whole core permeability

and pycnometer systems used in this study were installed at CSIR-CIMFR Dhanbad. It is a very fast, precise, and non-destructive determination of permeability and porosity of core samples under confining pressure.<sup>84,85</sup> Shale core samples having diameter 52 mm and length 150 mm were taken and polished on both ends with the help of a rotator machine. The core was fixed into the core holder, and it was allowed to maintain the desired confining pressure. An extremely delicate pulse-decay permeameter devoted to the setup was used to measure the trivial gas flow through the core. It is an unsteady-state permeameter intended to measure permeability in the range of 1 milli Darcy (mD) to 10 nano Darcies (10 nD).<sup>84,86</sup> The details of the procedure have been described by ref 4, 87.

## AUTHOR INFORMATION

### Corresponding Author

Vinod Atmaram Mendhe – CSIR-Central Institute of Mining and Fuel Research, Dhanbad 826015 Jharkhand, India;  
 ● [orcid.org/0000-0003-3212-8298](https://orcid.org/0000-0003-3212-8298); Email: [vamendhe@cimfr.nic.in](mailto:vamendhe@cimfr.nic.in), [vamendhe@gmail.com](mailto:vamendhe@gmail.com)

### Authors

Ranjit Gangadhar Khangar – Department of Applied Geology, Indian Institute of Technology (ISM), Dhanbad 826004 Jharkhand, India

Alka Damodhar Kamble – Department of Chemical Engineering, Indian Institute of Technology (ISM), Dhanbad 826004 Jharkhand, India

Piyush Ranjan Das – Department of Applied Geology, Indian Institute of Technology (ISM), Dhanbad 826004 Jharkhand, India

Priyanka Shukla – CSIR-Central Institute of Mining and Fuel Research, Dhanbad 826015 Jharkhand, India; AcSIR—Academy of Scientific and Innovative Research, Ghaziabad 201002 Uttar Pradesh, India

Mollika Bannerjee – Department of Applied Geology, Indian Institute of Technology (ISM), Dhanbad 826004 Jharkhand, India

Atul Kumar Varma – Department of Applied Geology, Indian Institute of Technology (ISM), Dhanbad 826004 Jharkhand, India

Complete contact information is available at:

<https://pubs.acs.org/10.1021/acsomega.1c03340>

### Notes

The authors declare no competing financial interest.

## ACKNOWLEDGMENTS

The authors are thankful to Dr. P. K. Singh, Director, CSIR-CIMFR Dhanbad, and Prof. Rajiv Shekhar, Director, IIT (ISM), Dhanbad, for granting permission to publish this paper. The authors are also thankful to the Ministry of Coal (MoC), Govt. of India, via Grant No. CE(EoI)/30 for funding Grant-in-Aid S&T [CE(EoI)/30] project on the “Shale gas potentiality evaluation of Damodar Basin of India” under which this research work was carried out.

## REFERENCES

(1) Montgomery, S. L.; Jarvie, D. M.; Bowker, K. A.; Pollastro, R. M. Mississippian Barnett Shale, Fort Worth Basin, northcentral Texas: Gas-shale play with multi - trillion cubic foot potential. *AAPG Bull.* **2005**, *89*, 155–175.

(2) Mendhe, V. A.; Kamble, A. D.; Bannerjee, M.; Mishra, S.; Sutay, T. Coalbed Methane: Present Status and Scope of Enhanced Recovery Through CO<sub>2</sub> Sequestration in India. In *Carbon Utilization*; Springer, 2017; pp 183–203.

(3) Mendhe, V. A.; Mishra, S.; Khangar, R. G.; Kamble, A. D.; Kumar, D.; Varma, A. K.; Singh, H.; Kumar, S.; Bannerjee, M. Organopetrographic and pore facets of Permian shale beds of Jharia Basin with implication to shale gas reservoir. *J. Earth Sci.* **2017**, *28*, 897–916.

(4) Mendhe, V. A.; Mishra, S.; Varma, A. K.; Kamble, A. D.; Bannerjee, M.; Singh, B. D.; Sutay, T. M.; Singh, V. P. Geochemical and petrophysical characteristics of Permian shale gas reservoirs of Raniganj Basin, West Bengal, India. *Int. J. Coal Geol.* **2018**, *188*, 1–24.

(5) Mishra, S.; Mendhe, V. A.; Varma, A. K.; Kamble, A. D.; Sharma, S.; Bannerjee, M.; Kalpana, M. S. Influence of organic and inorganic content on fractal dimensions of Barakar and Barren Measures shale gas reservoirs of Raniganj basin, India. *J. Nat. Gas Sci. Eng.* **2018**, *49*, 393–409.

(6) Curtis, J. B. Fractured Shale-Gas Systems. *AAPG Bull.* **2002**, *86*, 1921–1938.

(7) Jarvie, D. M.; Hill, R. J.; Ruble, T. E.; Pollastro, R. M. Unconventional shale gas systems: the Mississippian Barnett shale of north-central Texas as one model for thermogenic shale-gas assessment. *AAPG Bull.* **2007**, *91*, 475–499.

(8) EIA-Energy Information Administration, USA. World Shale Gas Resources: An Initial Assessment of 14 Regions Outside the United States, EIA, 2011.

(9) EIA-Energy Information Administration, USA. Annual Energy Review. [2017-09-10], 2012.

(10) Mazur, K. Economics of shale gas. <http://www.energybiz.com/article/12/10/economics-shale-gas> (accessed Aug 14, 2015).

(11) Mendhe, V. A.; Mishra, S.; Varma, A. K.; Kamble, A. D.; Bannerjee, M.; Sutay, T. Gas reservoir characteristics of the Lower Gondwana shales in Raniganj Basin of Eastern India. *J. Pet. Sci. Eng.* **2017**, *149*, 649–664.

(12) Abouelresh, M. O. An integrated characterization of the porosity in Qusaiba Shale, Saudi Arabia. *J. Pet. Sci. Eng.* **2017**, *149*, 75–87.

(13) Chen, Q.; Zhang, J.; Tang, X.; Li, W.; Li, Z. Relationship between pore type and pore size of marine shale: An example from the Sinian–Cambrian formation, upper Yangtze region, South China. *Int. J. Coal Geol.* **2016**, *158*, 13–28.

(14) Ahmadv, R. S. O. Microtextural, Elastic and Transport Properties of Source Rocks. Ph.D. Thesis, Stanford University, 2011.

(15) Ross, D. J.; Bustin, R. M. Shale gas potential of the lower jurassic gordondale member, northeastern British Columbia. *Bull. Can. Pet. Geol.* **2007**, *55*, 51–75.

(16) Aringhieri, R. Nanoporosity characteristics of some natural clay minerals and soils. *Clays Clay Miner.* **2004**, *52*, 700–704.

(17) Wang, L.; Torres, A.; Xiang, L.; Fei, X.; Naido, A.; Wu, W. A technical review on shale gas production and unconventional reservoirs modeling. *Nat. Resour.* **2015**, *6*, 141–151.

(18) Sondergeld, C. H.; Ambrose, R. J.; Rai, C. S.; Moncrieff, J. *Micro-Structural Studies of Gas Shales*; Society of Petroleum Engineers: Richardson, 2010.

(19) Spears, D. A. The fissility of some Carboniferous shales. *Sedimentology* **1976**, *23*, 721–725.

(20) Bustin, R. M.; Clarkson, C. R. Geological controls on coalbed methane reservoir capacity and gas content. *Int. J. Coal Geol.* **1998**, *38*, 3–26.

(21) Mendhe, V. A.; Kamble, A. D.; Bannerjee, M.; Mishra, S.; Mukherjee, S.; Mishra, P. Evaluation of shale gas reservoir in Barakar and Barren Measure formations of north and south Karanpura basins, Jharkhand. *J. Geol. Soc. India* **2016**, *88*, 305–316.

(22) Varma, A. K.; Mishra, D. K.; Samad, S. K.; Prasad, A. K.; Panigrahi, D. C.; Mendhe, V. A.; Singh, B. D. Geochemical and organopetrographic characterization for hydrocarbon generation from Barakar Formation in Auranga Basin, India. *Int. J. Coal Geol.* **2018**, *186*, 97–114.

(23) Mastalerz, M.; Schimmelmann, A.; Drobniak, A.; Chen, Y. Porosity of Devonian and Mississippian New Albany Shale across a

maturation gradient: insights from organic petrology, gas adsorption, and mercury intrusion. *AAPG Bull.* **2013**, *97*, 1621–1643.

(24) Chen, P.; Han, Q.; Ma, T. S.; et al. The mechanical properties of shale based on micro-indentation test. *Pet. Explor. Dev.* **2015**, *42*, 723–732.

(25) Painter, P. C.; Snyder, R. W.; Starsinic, M.; Coleman, M. M.; Kuehn, D. W.; Davis, A. Concerning the application of FTIR to the study of coal: a critical assessment of band assignments and the application of spectral analysis programs. *Appl. Spectrosc.* **1981**, *35*, 475–485.

(26) Kuehn, D. W.; Snyder, R. W.; Davis, A.; Painter, P. C. Characterization of vitrinite concentrates. 1. Fourier Transform infrared studies. *Fuel* **1982**, *61*, 682–694.

(27) Sobkowiak, M.; Painter, P. C. Determination of the Aliphatic and Aromatic CH Contents of Coals by FT-i.r.: Studies of Coal Extracts. *Fuel* **1992**, *71*, 1105–1125.

(28) Mastalerz, M.; Bustin, R. M.; Lamberson, M. N. Variation in chemistry of vitrinite and semifusinite as a function of associated inertinite content. *Int. J. Coal Geol.* **1993**, *22*, 149–162.

(29) Mastalerz, M.; Wilks, K. R.; Bustin, R. M. Variation in vitrinite chemistry as a function of associated liptinite content; a microprobe and FT-i.r. investigation. *Org. Geochem.* **1993**, *20*, 555–562.

(30) Ibarra, J.; Munoz, E.; Moliner, R. FTIR Study of the Evolution of Coal Structure during the Coalification Process. *Org. Geochem.* **1996**, *24*, 725–735.

(31) Guo, Y.; Bustin, R. M. FTIR spectroscopy and reflectance of modern charcoals and fungal decayed woods: implications for studies of inertinite in coals. *Int. J. Coal Geol.* **1998**, *37*, 29–53.

(32) Ganz, H.; Kalkreuth, W. Application of infrared spectroscopy to the classification of kerogen types and the evolution of source rock and oil shale potentials. *Fuel* **1987**, *66*, 708–711.

(33) Kister, J.; Guiliano, M.; Largeau, C.; Derenne, S.; Casadevall, E. Characterization of chemical structure, degree of maturation and oil potential of Torbanites (type I Kerogens) by quantitative FTIR spectroscopy. *Fuel* **1990**, *69*, 1356–1361.

(34) Lin, R.; Ritz, G. P. Reflectance FT-IR microspectroscopy of fossil algae contained in organic-rich shales. *Appl. Spectrosc.* **1993**, *47*, 265–271.

(35) Landais, P. Statistical determination of geochemical parameters of coal and kerogen macerals from transmission micro-infrared spectroscopy data. *Org. Geochem.* **1995**, *23*, 711–720.

(36) Chen, T.; Goodway, W. N.; Zhang, W.; Potocki, D.; Uswak, G.; Calow, B.; Gray, F. D. In *Integrating Geophysics, Geology and Petrophysics: A 3D Seismic AVO and Borehole/Logging Case Study*, Geo-Triad Meeting Abstracts, 1998; pp 316–319.

(37) Petsch, S. T.; Berner, R. A.; Eglinton, T. I. A field study of the chemical weathering of ancient sedimentary organic matter. *Org. Geochem.* **2000**, *31*, 475–487.

(38) Mendhe, V. A.; Mishra, S.; Singh, A. P.; Kamble, A. D.; Bannerjee, M.; Gupta, S. K. Management of Coalbed Methane and Coal Mine Produced Water for Beneficial Use in Damodar Basin of India. In *Water Resources Management*; Springer, 2018; pp 283–296.

(39) Varma, A. K.; Biswal, S.; Hazra, B.; Mendhe, V. A.; Misra, S.; Samad, S. K.; Singh, B. D.; Dayal, A. M.; Mani, D. Petrographic characteristics and methane sorption dynamics of coal and shaly-coal samples from Ib Valley Basin, Odisha, India. *Int. J. Coal Geol.* **2015**, *141–142*, 51–62.

(40) Singh, H. K.; Khanna, A. R. India's Energy Options: The Road Ahead an Analysis of The Prospects of Shale Gas in India's Energy Future. Indian Council for Research on International Economic Relations, ICRIER- Wadhvani Chair in India-US Policy Studies, 2012.

(41) Chalmers, G. R. L.; Bustin, R. M. Lower Cretaceous gas shales in north eastern British Columbia, part I: geological controls on methane sorption capacity. *Bull. Can. Pet. Geol.* **2008**, *56*, 1–21.

(42) Gasparik, M.; Ghanizadeh, A.; Bertier, P.; Gensterblum, Y.; Bouw, S.; Krooss, B. M. High-pressure methane sorption isotherms of black shales from the Netherlands. *Energy Fuels* **2012**, *26*, 4995–5004.

(43) Rexer, T. F. T.; Mathia, E. J.; Aplin, A. C.; et al. High-pressure methane adsorption and characterization of pores in Posidonia shales and isolated kerogens. *Energy Fuels* **2014**, *28*, 2886–2901.

(44) Guo, X.; Li, Y.; Liu, R.; et al. Characteristics and controlling factors of micropore structures of the Longmaxi shale in the Jiaoshi area, Sichuan basin. *Nat. Gas Ind. B* **2014**, *1*, 165–171.

(45) Javadpour, F. Nanopores and Apparent Permeability of Gas Flow in Mudrocks (Shales and Siltstone). *J. Can. Pet. Technol.* **2009**, *48*, 16–21.

(46) Kuila, U.; Prasad, M.; Derkowski, A.; McCarty, D. K. In *Compositional Controls on Mudrock Pore-Size Distribution: An Example from Nibrara Formation*, SPE Annual Technical and Exhibition, San Antonio, USA, Oct 8–10, 2012.

(47) Sengupta, N. A Revision of the Geology of the Jharia Coalfield with Particular Reference to Distribution of Coal Seams. Ph.D. Thesis, Indian School of Mines: Dhanbad, 1980.

(48) Chatterjee, G. C.; Ghosh, P. K. Tectonic framework of the peninsular Gondwana of India. *Rec. Geol. Surv. India* **1970**, *98*, 1–15.

(49) Basu, T. N.; Shrivastava, B. B. P. In *Structure and Tectonics of Gondwana Basins of India*, 5th International Gondwana Symposium, Wellington, New Zealand; Cresswell, M. M.; Vella, P., Eds.; Balkema: Rotterdam, 1981; pp 172–182.

(50) GSI; Rizvi, S. R. A. Auranga coalfield. *Mem. - Geol. Surv. India* **1977**, *88*, 182–186.

(51) Verma, R. P. In *Exploration Strategy for Preparing Master Plan for Reconstruction and Development of a Complex Coalfield in India*, 4th International Coal Exploration Symposium; Austin, R., Eds.; Miller Freeman: Sydney, NSW, 1983; pp 1–23.

(52) Coal India Limited. Coal Atlas of India. CMPDI, Ranchi, 1991.

(53) Verma, R. K.; Bhuin, N. C.; Mukhopadhyay, M. Geology, Structure and tectonics of Jharia Coal Field, India-A 3-D Model. *Geoexploration* **1979**, *17*, 305–324.

(54) Casshyap, S. M. Paleocurrents and paleogeographic reconstruction in the Barakar (Lower Gondwana) sandstones of peninsular India. *Sediment. Geol.* **1973**, *9*, 283–303.

(55) Varma, R. P.; Singh, V. K. In *A Chronology of Tectonics and Igneous Activity in Damodar Valley Coalfields*, Fourth International Gondwana Symposium (Vol. II); Laskar, B.; Raja Rao, C. S., Eds.; Hindustan Publ. Corp: Delhi, 1979; pp 901–907.

(56) Mukhopadhyay, G.; Mukhopadhyay, S. K.; Chowdhury, M. R.; Parui, P. K. Stratigraphic Correlation between Different Gondwana Basins of India. *J. Geol. Soc. India* **2010**, *76*, 251–266.

(57) Mastalerz, M.; Bustin, R. M. Application of reflectance micro-Fourier transform infrared spectrometry in studying coal macerals: comparison with other Fourier transform infrared techniques. *Fuel* **1995**, *74*, 536–542.

(58) Supaluknari, S.; Larkins, F. P.; Redlich, P.; Jackson, W. R. An FTIR Study of Australian Coals: Characterization of Oxygen Functional Groups. *Fuel Process. Technol.* **1988**, *19*, 123–140.

(59) Cerný, J. Structural dependence of CH bond absorptivities and consequences for FTIR analysis of coals. *Fuel* **1996**, *75*, 1301–1306.

(60) Başaran, Y.; Denizli, A.; Sakintuna, B.; Taralp, A.; Yürüm, Y. Bio Liquefaction/Solubilization of Low-Rank Turkish Lignites and Characterization of the Products. *Energy Fuels* **2003**, *17*, 1068–1074.

(61) Andreas, G.; Andreas, I.; Victoria, K. Study of low rank greek coals using FT-IR spectroscopy. *Energy Sources* **2003**, *25*, 995–1005.

(62) Debashis, B. Study of kinetics of iron minerals in coal by Fe-57 Mossbauer and FT-IR spectroscopy during natural burning. *Hyperfine Interact.* **2005**, *163*, 167–176.

(63) Manoj, B.; Kunjomana, A. G. FT-Raman Spectroscopic study of Indian Bituminous and sub-bituminous coal. *Asian J. Mater. Sci.* **2010**, *2*, 204–210.

(64) Narayanan, P.; Manoj, B. Study of changes to the organic functional groups of a high volatile bituminous coal during organic acid treatment process by FTIR spectroscopy. *J. Miner. Mater. Charact. Eng.* **2013**, *1*, 39–43.

(65) Sonibare, O. O.; Haeger, T.; Foley, S. F. Structural characterization of Nigerian coals by X-ray diffraction, Raman and FTIR spectroscopy. *Energy* **2010**, *35*, 5347–5353.



- (66) Yao, S. P.; Xue, C. Y.; Hu, W.; Cao, J.; Zhang, C. A comparative study of experimental maturation of peat, brown coal and subbituminous coal: Implications for coalification. *Int. J. Coal Geol.* **2006**, *66*, 108–118.
- (67) Stuart, B. H. *Infrared Spectroscopy: Fundamentals and Applications*; John Wiley & Sons, Inc., 2004.
- (68) Painter, P. C.; Starsinic, M.; Coleman, M. M. Determination of Functional Groups in Coal by Fourier Transform Interferometry. In *Fourier Transform Infrared Spectroscopy*; Ferraro, F. R.; Basile, L. G., Eds.; Academic Press: New York, 1985; pp 169–240.
- (69) Ganz, H.; Kalkreuth, W. IR classification of kerogen type, thermal maturation, hydrocarbon potential and lithological characteristics. *J. Southeast Asian Earth Sci.* **1991**, *5*, 19–28.
- (70) Yao, Y.; Liu, D.; Tang, D.; Tang, S.; Huang, W. Fractal characterization of adsorption-pores of coals from North China: an investigation on CH<sub>4</sub> adsorption capacity of coals. *Int. J. Coal Geol.* **2008**, *73*, 27–42.
- (71) Misra, S.; Varma, A. K.; Hazra, B.; Biswas, S.; Samad, S. K. The influence of the thermal aureole asymmetry on hydrocarbon generative potential of coal beds: Insights from Raniganj Basin, West Bengal, India. *Int. J. Coal Geol.* **2019**, *206*, 91–105.
- (72) Wang, S.; Tang, Y.; Schober, H.; Guo, Y.; Gao, W.; Lu, X. FTIR and simultaneous TG/MS/FTIR study of late Permian coals from southern China. *J. Anal. Appl. Pyrolysis* **2013**, *100*, 75–80.
- (73) Mastalerz, M.; Drobniak, A.; Strapoć, D.; Solano Acosta, W.; Rupp, J. Variations in pore characteristics in high volatile bituminous coals: Implications for coal bed gas content. *Int. J. Coal Geol.* **2008**, *76*, 205–216.
- (74) Sing, K. S. W.; Everett, D. H.; Haul, R. A. W.; Moscou, L.; Pierotti, R. A.; Rouquerol, J.; Siemieniowska, T. Reporting physisorption data for gas/solid systems with special reference to the determination of surface area and porosity. *Pure Appl. Chem.* **1985**, *57*, 603–619.
- (75) Zhong, L. W.; Zhang, H.; Yun, Z. R. Influence of specific pore area and pore volume of coal on adsorption capacity. *Coal Geol. Explor.* **2002**, *30*, 26–29.
- (76) IUPAC. Recommendations for the characterization of porous solids. *Pure Appl. Chem.* **1994**, *66*, 1739–1758.
- (77) Chen, L.; Ji, T.; Mu, L.; Shi, Y.; Wang, H.; Zhu, J. Pore size dependent molecular adsorption of cationic dye in biomass derived hierarchically porous carbon. *J. Environ. Manage.* **2017**, *196*, 168–177.
- (78) Feng, Y. Y.; Yang, W.; Chu, W. Coalbed Methane Adsorption and Desorption Characteristics Related to Coal Particle Size. *Chim. Phys. B* **2016**, *25*, No. 068102.
- (79) Pfeifer, P.; Avnir, D. Chemistry non integral dimensions between two and three. *J. Chem. Phys.* **1983**, *79*, 3558–3565.
- (80) Yang, F.; Ning, Z.; Liu, H. Fractal characteristics of shales from a shale gas reservoir in the Sichuan Basin, China. *Fuel* **2014**, *115*, 378–384.
- (81) Nie, H. K.; Zhang, J. C. Types and characteristics of shale gas reservoir: a case study of Lower Paleozoic in and around Sichuan Basin. *Pet. Geol. Exp.* **2011**, *33*, 232.
- (82) Yao, Y.; Liu, D.; Huang, W. Influences of igneous intrusions on coal rank, coal quality and adsorption capacity in Hongyang, Handan and Huaibei coalfield, North China. *Int. J. Coal Geol.* **2011**, *88*, 135–146.
- (83) Wang, F. P.; Reed, R. M. In *Pore Networks and Fluid Flow in Gas Shales*, SPE Annual Technical Conference and Exhibition, New Orleans, LA, 2009; SPE-124253.
- (84) Temco, Inc. Gas permeameter and porosimeter instruction manual (Model GPP). Tulsa, Oklahoma, USA, 1998.
- (85) Micromeritics Instruments. AccuPyc1330 pycnometer operator's manual. Part No. 133-42808-01, 2000.
- (86) Core Lab Instruments. Pulse decay permeameter operations manual. PSP/Rev-10003308, 1997.
- (87) Mendhe, V. A.; Mishra, P.; Varade, A. M. Coal seam reservoir characteristics for coalbed methane in North and South Karanpura coalfields, Jharkhand. *Gondwana Geol. Mag. Spec.* **2010**, *12*, 141–152.
- (88) Mendhe, V. A.; Bannerjee, M.; Varma, A. K.; Kamble, A. D.; Mishra, S.; Singh, B. D. Fractal and pore dispositions of coal seams with significance to coalbed methane plays of East Bokaro, Jharkhand, India. *J. Nat. Gas Sci. Eng.* **2017**, *38*, 412–433.
- (89) Yuan, Y.; Rezaee, R. Fractal analysis of the pore structure for clay bound water and potential gas storage in shales based on NMR and N<sub>2</sub> gas adsorption. *J. Pet. Sci. Eng.* **2019**, *177*, 756–765.
- (90) Yuan, Y.; Rezaee, R.; Verrall, M.; Hu, S.-Y.; Zou, J.; Testmanti, N. Pore characterization and clay bound water assessment in shale with a combination of NMR and low-pressure nitrogen gas adsorption. *Int. J. Coal Geol.* **2018**, *194*, 11–21.
- (91) Yuan, Y.; Rezaee, R.; Yu, H.; Zou, J.; Liu, K.; Zhang, Y. Compositional controls on nanopore structure in different shale lithofacies: A comparison with pure clays and isolated kerogens. *Fuel* **2021**, *303*, No. 121079.